Experimental and simulation studies of the shape and motion of an air bubble contained in a highly viscous liquid flowing through an orifice constriction.

B. Hallmark, C.-H. Cheng, J.F. Davidson

Department of Chemical Engineering and Biotechnology, Philippa Fawcett Drive, Cambridge. CB3 0AS. UK

Highlights

- When a gas bubble contained within a highly viscous Newtonian fluid flows through an orifice, a wide variety of bubble shapes are observed including highly-elongated 'crescent moons'.
- Predictions of bubble shape and velocity using OpenFOAM do not accurately match those obtained experimentally when an arithmetic mean viscosity is used.
- A new, logarithmically-weighted, arithmetic mean viscosity rule is presented and implemented within OpenFOAM: this enables accurate prediction of bubble shape and velocity.
- It is found that the accuracy of the simulation is critically dependent on mesh resolution and on the viscosity averaging method.
- Insight into the 3D structure of the bubble can be obtained from validated simulation work that would be difficult to acquire experimentally.

Abstract

This paper reports an experimental and computational study on the shape and motion of an air bubble, contained in a highly viscous Newtonian liquid, as it passes through a rectangular channel having a constriction orifice. The magnitude of the viscosity ratios, λ, and capillary numbers, Ca, explored is high: $5.5 \times 10^5 < \lambda < 3.9 \times 10^6$ and $2.9 < Ca < 35.9$ respectively. A multipass rheometer is used for the experimental work: air bubbles are suspended in 10 Pa s and 70 Pa s polybutene viscosity standards and passed through an orifice-plate geometry constructed within an optical flow-cell. High levels of bubble distortion are observed, including bubbles that resemble 'crescent moons'. Simulation work is carried out using an implementation of the volume of fluid method in the freely-available finite-volume computational fluid dynamics code OpenFOAM. Quantitative data pertaining to the motion and shape of the bubble was extracted from both the experimental and simulation work. Initially, a good match between numerical simulation and experimental work could not be obtained: this problem was alleviated by changing the viscosity averaging method from an arithmetic mean to a logarithmically-weighted arithmetic mean. Medium- and high-resolution simulations using this new viscosity averaging method were able to match experimental data with coefficients of determination, R^2, typically $0.898 < R^2 < 0.985$.

Keywords:

Multipass rheometer, two-phase flow, bubble motion, volume of fluid method, OpenFOAM, viscosity averaging rules.

© BH, CHC, JFD January 2019. Submitted to AIChEJ for consideration.

1. Introduction

Volcanic magma, the cement used to secure oil wells in fragile rock strata and whipped cream have one thing in common: their microstructure is formed by the presence of gas bubbles in a solidified liquid phase[1–3]. Whether the two-phase material was originally a dry foam, a wet foam or a bubbly liquid, the presence of gas bubbles significantly enhances the material properties of the resulting solid. Foaming polyurethane with carbon dioxide, for example, reduces its thermal conductivity by an order of magnitude[4] and foamed concrete has a substantially lower density than its non-foamed counterpart[2].

The ultimate properties of a voided material depend not only the properties of the gas and liquid phases used to form it, but also on the shape, size, distribution and number of bubbles within it. Since many of these voided micro-structured materials are formed by flow processes, it is of paramount importance to understand the behaviour of gas bubbles as they are transported by a liquid flow. Consequently, for many decades, physicists and engineers have been researching the behaviour of bubbly flows. They have discovered, for example, that the dynamics of single bubbles[5] and bubble swarms[6] are significantly different, that bubbles can change size over time due to mass transfer from gas to liquid and *vice versa*[7,8] and that bubbles can break apart and coalesce[9].

The precursors to polymer foams, volcanic magmas and many food products typically have a very high viscosity liquid phase. For flows of these materials, inertial effects are typically negligible and the dominant factors that affect the shape and size of bubbles are viscous and surface tension forces. The capillary number, Ca, describes the ratio between these two forces, with surface tension effects becoming negligible as $Ca \to \infty$. Studies of bubble dynamics at high capillary number have revealed a broad variety of bubble shapes, including long slender entities with cusped tips[10], aerofoil-shaped bubbles[11], and bubbles with either 'long' or 'short' tails[12].

In tandem with experimental work, theoreticians have endeavoured to produce mathematical models of bubble shape. This body of research has contributed substantial amounts of fundamental understanding into how the experimentally-observed bubble shapes are formed. For example, slender body theory[13] describes the deformation of droplets and bubbles as $Ca \to \infty$; this has been extended such that droplet deformation can now be understood at arbitrary capillary number[14]. The experimental observation of sharp bubble tips, or cusps, has been explained theoretically[15–17] and the behaviour of bubbles in complex geometries, such as rounded constrictions, has been studied computationally[18].

The ability to study two-phase flows computationally has enabled investigation into bubble motion and deformation in complex engineering geometries that would not be amenable to analytical approaches. A number of numerical techniques exist[19,20], forming part of the larger subject of computational fluid dynamics (CFD): these include lattice-Boltzmann methods, the level-set method, the boundary element

method and the volume of fluid (VoF) method. All these techniques have been used with great efficacy to examine numerous multiphase flow problems.

The dynamics of a single bubble rising in a viscous medium under the action of buoyancy was investigated in great detail experimentally[5] in the 1970s. In recent years, these experiments have been used as benchmark cases for numerical simulations[21–24]. These simulations have typically yielded excellent agreement with the original experimental work over a wide range of Reynolds numbers, Re, $0.1 < Re < 10^4$, and viscosity ratios, λ, $10 < \lambda < 5 \times 10^4$. Here, λ is defined as the ratio between the continuous phase viscosity and the dispersed phase viscosity. A variety of numerical methods were used in these studies including the VoF method[21], the level-set method[25], a combined level-set and VoF method[24] and the front-tracking method[22,23].

CFD has also been used to examine the behaviour of both bubbles and immiscible liquid droplets as they flow through microchannels: the numerical approach is identical in both cases. Typically, inertia is less important in these flow regimes with the bubble, or droplet, behaviour being characterised by Ca and λ. The formation and transport of immiscible liquid droplets in T-junction devices is explored using the VoF method and successfully compared to experimental data[26]. This study examines $0.01 < \lambda < 15$ and $10^{-3} < Ca < 0.5$ and gives a good summary of other microdroplet simulation studies. The motion of gas slugs, Taylor bubbles, in circular- and square-sectioned microchannels has also been studied[27] using the VoF method with $\lambda \sim 5.4 \times 10^4$ and $Ca \sim 1$: the authors note both excellent agreement with experimental data and insight being gained into micro-scale heat and mass transfer phenomena. Similarly good agreement to benchmark experiments was obtained by Hoang and co-workers[28], who examined bubbles in T-junction microchannels with $\lambda \sim 50$ and $10^{-3} < Ca < 0.1$ and Khodoparasat and co-workers[29], who studied the behaviour of small bubbles in circular microchannels with $\lambda \sim 3 \times 10^4$ and $Ca \sim 0.01$.

This paper is intended to contribute additional experimental data concerning the motion of air bubbles transported in a flow of highly viscous liquid contained in rectangularly-sectioned geometries of varying cross section. The viscosity ratios and capillary numbers are both very high: here, $5.5 \times 10^5 < \lambda < 3.9 \times 10^6$ and $2.9 < Ca < 35.9$. These experiments, described in Section 0, form part of a larger body of work by the same authors that is currently under consideration for publication. In this study, the experiments are used as benchmark cases for CFD studies using the VoF method, described in Section 3. Some minor adjustments were required to the viscosity averaging law used within the VoF method in order to obtain a good match between experimental data and numerical simulation: these comparisons are discussed in Section 4 and some analysis is presented concerning the strengths and weaknesses of the viscosity law modification.

2. Experimental methods and materials

2.1 The multipass rheometer

The multipass rheometer (MPR)[30] is a highly versatile[31] rheometric platform that was invented at the University of Cambridge in the mid-1990s. MPRs are, in essence, fully-enclosed capillary rheometers, capable of operating at elevated temperature and pressure. They can be configured to operate in a variety of ways and, as such, can measure a wide range of rheological and material property data. 'Traditional' capillary rheometry can be undertaken, which relies on taking measurements of differential pressure across a (typically stainless steel) capillary of known geometry whilst a fluid flows through it. This yields viscosity data on the liquid under investigation, which can be anything from a polymer melt[32] to a printing ink[33]. Use of beryllium capillaries in place of stainless steel allow *in-situ* 'X'-ray diffraction measurements to be taken of the material within the flow chamber. This can yield structural information about the fluid giving insight into, for example, the onset flow-induced crystallisation[34] or the phase changes experienced by cocoa butter as it is processed[35].

Of relevance to the study presented here is incorporation of an optical flow cell within the MPR in place of a solid capillary. This provides the ability to visualise the fluid flow allowing, for example, measurement of stress fields in flowing, birefringent, materials[36,37], direct observation of flow-induced crystallisation[38] or direct observation of bubble behaviour in polymer foams[39] or foamed food materials[40]. The work presented in this paper used an MPR configured with an optical flow cell containing an orifice plate.

The MPR contains two pistons and cylinders, the pistons moving to-and-fro synchronously, so as to induce to-and-fro motion of liquid through an orifice connected to the two cylinders. The orifice was constructed of stainless steel, but held in place by quartz glass windows such that bubbles in the liquid could be observed.

A schematic diagram of the essential parts of the (MPR) is given in Figure 1(A). The region shown in white represents the location of the viscous liquid; the orifice plate test section is shown in black in the centre of this region. Two servo-hydraulic pistons, indicated in black, move synchronously in a to-and-fro motion thus causing the viscous liquid to flow through the orifice plate.

The black, dashed, square surrounding the orifice plate represents the region of observation, illuminated by an LED light source (Thorlabs MCWWHCP1) and observed using a high-speed CMOS camera (Basler acA1300-200HC). The light source and camera were positioned to observe the flow constriction such that the axis joining the light source and camera was normal to the plane of the diagram.

<FIGURE 1>

The flow is fully three-dimensional. The fluid and the orifice plate are contained by two quartz glass windows: these windows are 1 mm apart in the plane of diagram and hence set the thickness of the flow channel in the observation region. Dimensions of the observation region, including the orifice plate, are shown in Figure 1(B). Situated above and below the observation region are two cylindrical fluid reservoirs in which are placed the pistons. The pistons are a sliding fit within these reservoirs, with both pistons and reservoirs being 10 mm in diameter.

Two viscous liquids were used for the experimental work: both liquids were Newtonian polybutene oils, commonly used as viscosity standards. The first (Brookfield viscosity standard B7300) was quoted to have a viscosity of 70.0 Pa s at 25 °C with the second (Brookfield viscosity standard XXXX) having a viscosity of 10.0 Pa s at the same temperature.

2.2 Experimental procedure

The viscous liquid was loaded into the test section of the MPR, shown in white in **Error! Reference source not found.**(A), taking care not to accidentally entrain any bubbles of air. A hypodermic syringe was then used to inject a single air bubble, approximately 500 μm in diameter, into the fluid within the observation region. This bubble was suspended stably in the liquid, with effects due to Ostwald ripening and buoyancy being longer than the observation timeframe due to the highly viscous nature of the liquid.

The upper and lower pistons were moved synchronously and in phase with one another such that either an up-flow or downflow of fluid was created within the observation region. The piston velocities ranged from 0.01 to 10 mm/s, corresponding to volumetric flow rates ranging between 0.785 to 785 mm^3/s. This fluid flow transported the bubble towards, through, and away from the orifice and the high-speed camera was used to record images of this bubble motion.

The flow regime within the MPR was classified using the capillary number, Ca. This parameter gives a measure of the relative effects of viscous forces and surface tension forces. It is written in terms of the liquid-phase viscosity, μ_l, a characteristic velocity, u and the interfacial tension between the gas and liquid phases, σ, *viz*

$$Ca = \frac{\mu_l u}{\sigma} \tag{1}$$

The characteristic velocity, u, was taken to be the centre-line velocity. A analytical method to calculate the ratio between the average and centre-line velocity in steady, laminar, flows through a ducts of rectangular cross-section[41] was used to calculate u from the volumetric flow-rate. This is described in more detail in Appendix A.

2.3 Image analysis

Quantitative information pertaining to the shape and motion of the bubble as it passed through the observation region was obtained using image analysis. Two open source image analysis codes were used for this task: FIJI[42] and Icy[43]. Within Icy, the 'Active Cells' plug-in[44] was used to obtain sets of co-ordinates that defined the location of the bubble interface. The 'Active Cells' tool made use of the fast active contour method[45].

Numerical data extracted from image analysis were processed further using Origin® (OriginLab) to obtain data on the bubble motion and to quantitative measurements of the bubble shape. Two shape metrics were used: roundness and convexity ratio[46]. These two metrics are commonly used for discrete particles and are illustrated schematically in Figure 2.

<FIGURE 2>

2.4 Data analysis

The 'goodness of fit' between the experimentally-observed and theoretically-predicted metrics of bubble motion and shape were compared using the coefficient of determination, R^2. A number of different formulations for this parameter exist[47].The exact formulation used here is

$$R^2 = 1 - \frac{\sum_{i=1}^{n}(y_i - f_i)^2}{\sum_{i=1}^{n}(y_i - \bar{y})^2} \quad \textbf{(2)}$$

Here, a set of experimentally-observed parameters, y_i, is compared to a theoretically-predicted predicted set of the same parameters, f_i, and to the arithmetic mean value of the experimental parameter set, $\bar{y}$. In this work, the parameter set will be one of the metrics used to describe either the bubble motion or the bubble shape.

3. Computational methods and theory

3.1 The volume of fluid (VoF) method

Only the essential components of the VoF method that are relevant to this research are presented here: for a more detailed description the reader is advised to consult one of the many excellent text books[19] or review papers[20] on the subject. The VoF method assumes that the flow is pseudo single-phase, regardless of the presence of multiple phases, and that the velocity and pressure fields within the fluid can be calculated by solving the Navier-Stokes (N-S) equations, Equation (3), using a suitable numerical algorithm. OpenFOAM uses the finite volume method to discretise the N-S equations, and offers a choice of pressure-velocity coupling schemes including the iterative semi-implicit pressure-linked

equations (SIMPLE) method[48], the non-iterative pressure-implicit split-operator (PISO) scheme[49] or a hybrid approach.

$$\frac{D}{Dt}(\rho\mathbf{v}) = \bar{\rho}\mathbf{g} + \bar{\mu}\nabla^2\mathbf{v} - \boldsymbol{\nabla}p + \mathbf{F_i} \quad \textbf{(3)}$$

For the work presented here, the flow was assumed to be compressible hence the inclusion of density within the total derivative: the continuity and energy equations are also solved in parallel with the N-S equations. Compressibility effects are usually neglected for slow, viscous, flows however the magnitude of the pressure drop through the orifice plate, and the consequent effect of this on the bubble volume, warrants their inclusion. The force due to interfacial tension on the boundary between the two phases is accounted for by vector $\mathbf{F_i}$: this is explained in more detail later.

The density and viscosity values, $\bar{\rho}$ and $\bar{\mu}$, are weighted by a parameter that indicates which phase is present within a given calculation cell, α: this parameter is termed the phase fraction parameter. Use of the phase fraction parameter allows the pseudo single-phase approach to be used for multiple phases. Typically, for a two-phase gas-liquid flow, $\alpha = 1$ in the liquid phase and $\alpha = 0$ in the gas phase. The only location where $0 < \alpha < 1$ is on a phase boundary. Conventionally, the weighting used for the density and viscosity is the arithmetic mean, *viz*

$$\bar{\rho} = \alpha\rho_l + (1-\alpha)\rho_g \quad \textbf{(4)}$$

$$\bar{\mu} = \alpha\mu_l + (1-\alpha)\mu_g \quad \textbf{(5)}$$

The phase fraction parameter, α, must be transported by the flow for the VoF method to work: an analogy here is to think of how individual bubbles within a liquid are transported by a bulk liquid flow. Phase fraction transport is achieved by coupling an extra partial differential equation (PDE) into the numerical scheme: this PDE takes the form

$$\frac{D\alpha}{Dt} = 0 \quad \textbf{(6)}$$

The numerical solution of Equation (6) can result in the interface between the two fluid phases being subject to artificial numerical diffusion. It is, therefore, usual to include correction terms in Equation (6) termed 'interface compression parameters' to prevent this from happening. The concept underlying interface compression is explained by So and co-workers[50] and the exact form used in OpenFOAM is described in a number of publications, for example that by Klostermann and co-workers[51].

The effect of interfacial tension needs to be considered on any interface between the phases, where $0 < \alpha < 1$. The method used in OpenFOAM is the 'constant surface force method' due to Brackbill and co-workers[52]. This assumes that the interfacial force vector, $\mathbf{F_i}$, can be calculated on a volumetric basis *via* knowledge of the interface curvature, $\boldsymbol{\kappa}$, the interfacial tension, σ, and the value of the phase fraction, α, *viz*

$$\mathbf{F_i} = \boldsymbol{\kappa}\sigma(\nabla\alpha) \tag{7}$$

with curvature being given by

$$\boldsymbol{\kappa} = \nabla\left(\frac{\nabla\alpha}{|\nabla\alpha|}\right) \tag{8}$$

Use of the arithmetic mean density and viscosity, Equations (4) and (5), although straightforward is not necessarily correct. Indeed, it can be shown that for a planar shear flow of two immiscible fluids, the harmonic mean is the correct average to use *i.e.*

$$\bar{\mu} = \frac{1}{\dfrac{(1-\alpha)}{\mu_g} + \dfrac{\alpha}{\mu_{l_l}}} \tag{9}$$

Use of the harmonic mean in place of the arithmetic mean was first highlighted when considering heat transfer through two materials of differing thermal conductivity[53]. Furthermore, it has been demonstrated that the harmonic mean viscosity is an appropriate parameter to use in certain classes of multiphase flow problem[20], such as the flow of two immiscible liquids in a 2D Hele-Shaw cell[54].

An alternative averaging method is tested in this paper, intended for use where the viscosity ratio between the two fluids is high: in this case between six and seven orders of magnitude. Rather than using either the arithmetic or harmonic means directly, a logarithmically-weighted arithmetic mean viscosity is proposed, *viz*

$$\bar{\mu} = \exp\big(\alpha\ln(\mu_l) + (1-\alpha)\ln\big(\mu_g\big)\big) \tag{10}$$

The variation of $\bar{\mu}$ as a function of α for each of the three averaging rules is illustrated in Figure 3. Examination of this Figure reveals that use of the logarithmically-weighted arithmetic mean avoids large changes of $\bar{\mu}$ with small changes of α, which is a characteristic of both the arithmetic and harmonic means.

<FIGURE 3>

Typically, the numerical solution of the set of PDEs corresponding to a VoF problem is done transiently. In order to obtain a convergent solution, the solution timestep, Δt, is adjusted adaptively according to the Courant-Friedrich-Lewy criterion[55]. Convergence behaviour is set by the dimensionless Courant number, Co, which relates Δt to the velocity magnitude, u, and to a characteristic length, Δx, at a given point in the computational domain *viz*

$$Co = \frac{u\Delta t}{\Delta x} \tag{11}$$

If Co, hence Δt, is calculated at every point in the computational domain, then the smallest value of Δt is usually chosen.

3.2 Simulation of bubble motion using OpenFOAM

Two sets of simulation work, termed 'Scenarios', are presented here: both Scenarios are directly comparable to the experimental work. The first Scenario concerned the motion of an air bubble transported through an orifice constriction in a continuous phase having a viscosity of 70 Pa s: the volumetric flow rate of the continuous phase was 7.85 mm^3/s. The second scenario pertained to the same flow geometry but with a continuous phase of viscosity 10 Pa s and volumetric flow rate 78.5 mm^3/s.

Four sets of simulations were done for each Scenario: one 'high resolution' simulation that used the arithmetic mean viscosity law, Equation (5), and simulations at 'low', 'medium' and 'high' resolution that used the logarithmically-weighted arithmetic mean viscosity, Equation (10). It was found at an early stage that convergence could not be obtained using the harmonic mean viscosity law, Equation (9). Image analysis, identical to that described in Section 0, was carried out on the resulting graphical sequences of predicted bubble motion. This yielded quantitative information on bubble motion and bubble shape that could be directly compared to the experimental measurements.

The open-source CFD code OpenFOAM[56] was used for the simulations. This code, first developed in 1998 and now on version 6, consists of a sophisticated suite of numerical algorithms that can be used to solve many different classes of flow problem using the finite volume method[57]. The solver that was used and modified in this work, `compressibleInterDyMFoam` from OpenFOAM version 2.3.1, can be used for three-dimensional compressible two-phase flow problems and incorporates dynamic mesh refinement.

All simulation work was carried out on a Linux® cluster consisting of 20 Supermicro® servers, with each server containing twin 8-core Intel® Xeon processors clocked at 2.7 GHz. The cluster had a total of 320 cores and 736 GB of RAM. Inter-process communication and remote direct memory access was provided by a 40 Gb/s Infiniband® network.

Figure 4(A) illustrates schematically the calculation geometry that was used in plan and side view. Figure 4(B) is an example of the mesh that resulted, generated using OpenFOAM's `blockMesh` utility.

<FIGURE 4>

Dimensional data for the calculation geometry are given in Table 1, with Table 2 detailing the number of edge divisions that were used in each of the segments shown in Figure 4(A). The slight change to the *y*-location of points E-H when compared to Figure 1(B) was to account for some of the minor defects present in the physical geometry due to wear and tear. Sets of faces, upon which boundary conditions could be imposed, were defined from groups of edges: face definitions are given in Table 3.

<TABLE 1>

<TABLE 2>

<TABLE 3>

The simulations were carried out in two steps. Firstly, a single-phase problem was solved so that velocity and pressure fields for the entire calculation geometry could be estimated at the desired volumetric flowrate and for the chosen continuous phase viscosity. These data were also used to estimate the internal pressure of the bubble: this was taken as the continuous phase pressure at the co-ordinates of the bubble centre. Then, these velocity and pressure data were used as initial conditions for the two-phase flow simulation. If this first step was omitted, and the two-phase problem was attempted using crude estimates of the internal bubble pressure and of the continuous phase velocity and pressure fields, the coupling between the pressure field and the shape and size of the bubble would cause the solution algorithm to diverge.

Material property data are given in Table 4 and the boundary conditions used in the single-phase problem are shown in Table 5 and Table 6: initial conditions are shown in Table 7. No mesh refinement was necessary for the single-phase problem and sufficiently accurate solutions for the velocity and pressure fields were obtained after 0.1 s of transient simulation time. Split over 90 cores, this simulation took a little over two minutes of 'wall time' with $Co = 1$.

<TABLE 4>

<TABLE 5>

<TABLE 6>

<TABLE 7>

The pressure, velocity, temperature and phase fraction fields resulting from the single-phase simulation were used as the combined initial and boundary condition definitions for the two-phase problem. The

phase fraction field was then manipulated using OpenFOAM's `setFields` command to place a spherical 'bubble' of dispersed phase at a specified location within the continuous phase. The radius and location of this region corresponded to the location and size of the bubble at the start of each of the experiments and was obtained using image analysis: these data are given in Table 8. The resolution of each of the simulations was set by adjusting the parameters in OpenFOAM's `dynamicMeshDict` file: the parameters used for each of the three resolutions are given in Table 9. Each of the simulations was then decomposed into a specified number of domains using the SCOTCH algorithm[58,59] invoked with OpenFOAM's `decomposePar` command and the subsequent problem solved using OpenFOAM's `compressibleInterDyMFoam` solver using a 'maximum' Courant number. If solver divergence occurred, the solver was restarted from the most recent solution file using a 'minimum' Courant number. Judgement was applied as to when an appropriate stage in the simulation had been reached to increase the Courant number back to the maximum value. Domain decomposition and solver data are given in Table 10. Once convergence had been attained, Paraview[60] was used to produce phase fraction contour plots for subsequent image analysis.

<TABLE 8>

<TABLE 9>

The OpenFOAM configuration files, including those used to set the numerical algorithm parameters `fvSolution` and `fvSchemes` are available in the supplementary information pack that accompanies this paper[1].

4. Results and discussion

4.1 Scenario 1 – 70 Pa s continuous phase

Four representative experimental images of an air bubble being transported towards, through, and away from a constriction orifice are shown in Figure 5. The continuous phase was 70 Pa s polybutene and the flow-rate of polybutene was 7.85 mm^3/s. Based on the assumptions and calculations shown in Appendix A, the capillary number in the centre of the orifice was 25.1, falling to 2.9 in the centre of the MPR geometry far away from the orifice.

Also shown in this Figure are contour plots formatted in such a way that all locations where $\alpha \leq 0.1$ are shown in black: the reasons underlying this choice of α are given in a discussion later in this section. The timestep for each contour plot was selected such that the location of the most downstream edge of the region where $\alpha = 0.1$ was a close match to the most downstream edge of the bubble in the photographs. An exact match was not always possible due to the finite number of timesteps at which

[1] This supplementary information pack will be supplied should the paper be accepted for publication.

simulation data was saved. In the discussion that follows, the black areas in these contour plots will be referred to as the 'predicted bubble'.

<FIGURE 5>

Qualitative visual comparison between the shape of the bubble photographed during experiments and that of the predicted bubble reveal some interesting similarities and differences. The shape of the predicted bubble resulting from the solver using the arithmetic mean viscosity, Equation (5), run at high resolution does not match the experimental observations particularly well. As the predicted bubble approaches the orifice, it is noticeably more slender than its experimental counterpart and lacks the 'bulbous' shape at its most downstream point. Furthermore, the predicted bubble has a noticeable 'tail' as it passes through and away from the orifice, a feature that is not present experimentally. Finally, the predicted bubble at its most downstream location has quite a sizeable gas envelope without cusped ends: the experimental case shows a slender 'crescent moon' type bubble with sharply cusped tips.

These differences could be explained, in part, by considering the value of $\bar{\mu}$ for a given value of α. Using Equation (5), $\bar{\mu} = 7$ Pa s when $\alpha = 0.1$, a viscosity that is not representative of the gas phase despite the relatively 'low' value of the phase fraction. In order to obtain a more representative gas phase viscosity, for example $\bar{\mu} = 8 \times 10^{-5}$ Pa s, $\alpha = 1 \times 10^{-6}$. Even if simulations are run such that the lower and upper mesh refinement limits, shown in Table 9, bracket $\alpha = 1 \times 10^{-6}$, numerical error from solving the phase fraction transport equation results in poor prediction of the 'interface' location. Initial simulation work exploring this problem was the motivating factor behind the development of a viscosity averaging law that could yield gas-like values of $\bar{\mu}$ for relatively 'large' values of α. The harmonic mean viscosity, Equation (9), achieves this since $\bar{\mu} = 5 \times 10^{-5}$ Pa s when $\alpha = 0.8$: simulations typically diverged, however, after only a few tens of iterations when this law was used. A possible explanation for this is discussed in Section 4.3. If the logarithmically-weighted arithmetic mean is used, Equation (10), then $\bar{\mu} = 4.8 \times 10^{-5}$ Pa s when $\alpha = 0.1$. Furthermore, as shown in Figure 3, the logarithmically-weighted arithmetic mean can result in range of $\bar{\mu}$ that spans essentially from the continuous phase to the discrete phase viscosities for numerically significant values of α, *i.e.* for $0.1 < \alpha < 0.9$.

The predicted bubble shapes resulting from the logarithmically-weighted mean viscosity, Equation (10), appear at first sight to be a closer match to the experimental photographs. At all resolutions, the initially 'bulbous' shape of the most downstream part of the bubble is predicted as the bubble enters the orifice. Furthermore, the predicted bubble shapes resulting from the medium- and high-resolution simulations continue to be a generally good match to the remaining three experimental images. No significant 'tail' is predicted, and an increasingly concave, cusped, shape is predicted as the bubble moves downstream of the orifice.

Quantitative comparison of the motion of the experimental and predicted bubble is shown in Figure 6: Figure 6(A) compares the motion of the bubble centroid and Figure 6(B) examines the motion of the most downstream location of the bubble, termed the 'front'. Quantitative comparison of the bubble shape, in terms of roundness and convexity measurements, are given in Figure 7(A) and Figure 7(B) respectively. Coefficients of determination that quantify the goodness of fit between the experimental data and the theoretical predictions of both motion and shape are given in Table 11.

<FIGURE 6>

<FIGURE 7>

<TABLE 11>

These numerical data reinforce the initial qualitative observations. The solver using the arithmetic mean viscosity law, Equation (5), makes a reasonable prediction of the movement of the bubble centroid with the qualitative trend being captured in Figure 6(A), with $R^2 = 0.889$. Predictions made with the same solver for the movement of the front of the bubble, Figure 6(B), ($R^2 = 0.562$) and for the shape metrics of roundness, Figure 7(A), ($R^2 = 0.195$) and convexity, Figure 7(B), ($R^2 = 0.540$) show significant deviation from the experimental case. In terms of these latter two metrics, the trend of both roundness and convexity is captured qualitatively but with a significant time-lag, which impacts the R^2 values.

The predicted motion and shape of the bubble using the logarithmically-weighted viscosity, Equation (8), seem to match the experimental data shown Figure 6 and Figure 7 very well. Interestingly, these Figures seem to suggest that the best description of both measurements of bubble motion are provided by the medium-resolution solution, but that the high-resolution solution captures the bubble shape more accurately. This observation is confirmed by the coefficients of determination: all predictions have significantly higher R^2 values than those from the solver using the arithmetic mean. Interestingly, these data support the notion that the medium-resolution solution is generally the most accurate: the predicted motion of the centre and front of the bubble have $R^2 = 0.988$ and $R^2 = 0.994$ respectively, and the roundness and convexity metrics have $R^2 = 0.919$ and $R^2 = 0.902$. The high-resolution solution only surpasses the accuracy of the medium-resolution solution with the prediction of bubble convexity, with R^2 =0.985.

The superior predictions of the medium-resolution solver are reassuring when data concerning the performance of the four simulations are examined. These data are given in Table 12.

<TABLE 12>

For the logarithmically-weighted viscosity law, the medium-resolution case converged in a little under a week using 90 cores, whereas the high-resolution case took a little over six weeks using 160 cores. The number of mesh cells in each case is rather low – just below 320,000 cells at medium resolution

and a little over 1.3 million cells at high resolution. In terms of a comparison, the high-resolution solution with the arithmetic mean viscosity law used a little over 2.1 million cells but only took ~17 hours to run when distributed on 160 cores. In all three of these cases, simulations were not making optimal use of the cluster: for the system configuration used, roughly 20,000 to 40,000 mesh cells per core ensured that the data transmission time *via* the Infiniband® network was smaller than the per-core calculation times.

When the data in Table 12 is examined more closely, it is evident that solutions using the logarithmically-weighted solver are timestep constrained. The high-resolution case has an average timestep two orders of magnitude smaller than the high-resolution solution using the arithmetic mean viscosity. The logarithmically-weighted solver takes ~646000 iterations to converge compared to the ~7500 iterations required by the arithmetic mean. Both simulations were run with $Co = 1$. This is interesting: on the assumption that the smallest mesh length-scale is similar in these two cases, then this observation infers that the largest velocity present at any iteration is two orders of magnitude higher when using the logarithmically-weighted viscosity rule compared to the arithmetic mean viscosity rule. The volumetric flow-rates of continuous phase are, however, the same. Further discussion of this anomaly is continued in Sections 4.2 and 4.3.

4.2 Scenario 2 – 10 Pa s continuous phase

A set of images comparing experimental observation and numerical prediction of bubble shape, similar to those given for Scenario 1, is shown in Figure 8. Now, the continuous phase viscosity was 10 Pa s and the volumetric flow rate of continuous phase was set to 78.5 mm^3/s. These conditions resulted in a capillary number of 35.9 in the centre of the orifice, falling to 4.2 in the centre of the MPR geometry far away from the orifice. As before, the predicted bubble shape is derived from phase fraction contour plots that are formatted such that all locations where $\alpha \leq 0.1$ appear in black.

<FIGURE 8>

Many of the qualitative observations that were made when discussing Figure 5 apply here. The shape of the predicted bubble resulting from the solver using the arithmetic mean viscosity, Equation (5), is still a poor match to the experimentally-observed bubble shape. The predicted shape of the bubble moving towards the orifice is markedly different to its experimental counterpart, with the most downstream location taking a ‘pointed’ shape rather than a ‘semi-bulbous’ shape. Predicted bubble shapes again feature a ‘tail’ that is not present experimentally. Furthermore, the shape of the predicted bubble’s gas envelope at its most downstream location now appears asymmetric and distorted: arguably a poorer prediction than was obtained for Scenario 1 and deviating significantly from that observed experimentally.

As before, the predicted bubble shapes resulting from the logarithmically-weighted mean viscosity, Equation (10), appear to match the experiments more closely. The low-resolution simulation is unable to capture the cusps that appear experimentally when the bubble is both located within the orifice and far downstream of the orifice. The medium- and high-resolution simulations, again, compare relatively favourably with their experimental counterparts. The predicted bubble shape at high resolution appears to match the experimental situation most closely: cusped bubble tips are predicted, as observed in the experiments, and the bubble shape far downstream of the orifice lacks the central 'lump' that is present in low- and medium-resolution simulations but not present experimentally.

Quantitative comparison of the motion of the experimental and predicted bubble is shown in Figure 9: Figure 9(A) compares the motion of the bubble centroid and Figure 9(B) examines the motion of the front of the bubble. Bubble shapes are compared in Figure 10: roundness data are shown in Figure 10(A) and convexity data in Figure 10(B). As before, coefficients of determination that quantify the goodness of fit between the experimental data and the theoretical predictions are given in Table 11.

<FIGURE 9>

<FIGURE 10>

When the trends in Figure 9 and Figure 10 are compared to those shown in Figure 6 and Figure 7, it appears that Scenario 2 is more challenging to simulate. The solver using the arithmetic mean viscosity law, Equation (5), makes comparable predictions to those in Scenario 1 of the movement of centroid ($R^2 = 0.889$) and front ($R^2 = 0.594$) of the bubble. The prediction of bubble roundness is significantly poorer for Scenario 2 ($R^2 = -0.145$), however the convexity prediction is better ($R^2 = 0.732$). Examination of the two plots in Figure 10 show the same trait that was shown in Figure 7: the trend of both roundness and convexity is captured qualitatively but with a significant time-lag, which impacts the R^2 values.

In a similar fashion to Scenario 1, the predictions of bubble shape and dynamics using the logarithmically-weighted viscosity, Equation (8), seem to match the experimental data better than those obtained using the arithmetic mean law. The low-, medium- and high-resolution solutions all predict the movement of the centroid and the front of the bubble with $R^2 > 0.9$. Prediction of the bubble shape, however, is less accurate than the results presented for Scenario 1. Bubble convexity is more accurately predicted than bubble roundness: for convexity $R^2 = 0.853$ at medium resolution and R^2=0.898 at high resolution, whereas for roundness $R^2 = 0.648$ at medium resolution and $R^2 = 0.734$ at high resolution.

This time, the high-resolution solution appears to be the most accurate based on the coefficient of determination in all metrics bar the movement of the front of the bubble. This latter quantity is better predicted by the medium resolution solution: $R^2 = 0.933$ at medium resolution *vs* $R^2 = 0.903$ at high resolution.

An important consequence of using a volumetric flowrate ten times higher than that in Scenario 1 is that the simulation end-time for Scenario 2 is ten times lower: 0.15 s compared to 1.5 s. This, in turn, results in significantly shorter model run times. If the simulation performance data for Scenario 2, contained in Table 12, is examined then some interesting observations can be made. In all cases more mesh cells are used than in Scenario 1: the most significant difference is for the high resolution logarithmically-weighted solver with ~2.4 million cells being used in Scenario 2 compared to ~1.4 million cells in Scenario 1.

Interestingly, the number of iterations required for all the simulations using the logarithmically-weighted viscosity law is roughly an order of magnitude less in Scenario 2 than in Scenario 1. Moreover, the average timestep values are slightly larger. This is despite an order of magnitude increase in average velocity, and the simulations being run at the same Courant number. As a comparison, note that the tenfold velocity increase has reduced the average timestep used in the arithmetic mean solution by the expected order of magnitude, suggesting that the smallest characteristic length in the mesh is broadly similar in both Scenario 1 and Scenario 2. These observations lead to the conclusion that the largest velocities present in the simulations using the logarithmically-weighted viscosity law are similar in both Scenario 1 and Scenario 2 and are therefore essentially insensitive to the velocity of the continuous phase.

4.3 Presence of anomalous velocities

An important observation stemming from both Scenario 1 and Scenario 2 related to the anomalous behaviour of the simulation timestep when the logarithmically-weighted viscosity rule was used. The key observations were that: (i) the average value of the timestep was between one and two orders of magnitude lower than for comparable simulations using the arithmetic mean viscosity law; (ii) that the average value of the timestep was seemingly insensitive to an order of magnitude increase in continuous phase volumetric flow-rate at constant Courant number; (iii) simulations were timestep limited, with the longest simulation runtime taking almost six weeks on 160 cores.

Some insight into these observations can be made by comparing the velocity fields present in two simulations of the same resolution at a comparable timestep but with different viscosity averaging methods. Both images shown in Figure 11. Velocity field data from numerical simulation (shown as arrows where the length of the arrow is directly proportional to velocity magnitude) superimposed onto the predicted location of a bubble. Flow is from bottom to top. (A) corresponds to the existing solver and (B) the modified solver. Note the presence of significant spurious currents in the modified solved and that the velocity magnitudes of these currents are significantly larger than the velocities in the centre of the orifice.Figure 11 are from Scenario 1 and superimpose the region where $\alpha \leq 0.1$, the ‘bubble’, shown in yellow, onto a plot of the velocity field shown as vector arrows. These arrows point in the flow direction and their length corresponds to the velocity magnitude at the arrow centre.

<FIGURE 11>

Figure 11(A) corresponds to the arithmetic mean viscosity law, Equation (3) and Figure 11(B) corresponds to the logarithmically-weighted law, Equation (8). It is immediately apparent from this Figure that there are anomalously large velocity vectors present in the interface region when the logarithmically-weighted viscosity law is used that are absent when the arithmetic mean viscosity is used. These velocity anomalies are orders of magnitude larger than the velocities present in the orifice, the point where the continuous phase moves fastest, thus providing an explanation for the seeming insensitivity of the simulation timestep on the volumetric flowrate for fixed Courant number.

At first sight, these anomalous velocities could be attributed to 'spurious currents', a well-documented phenomenon[20,61,62] that can be present in multiphase flow simulations that use continuum surface force models. These 'spurious currents' result from the discrete nature of the reconstructed gas-liquid interface in VoF solutions. These discretised interfaces are not smooth, resulting in slightly erroneous predictions of the interfacial force vector. In turn, these force imbalances result in unphysical fluid motion, typically vortex-like in nature. Close examination of Figure 11(B) does not reveal vortex-like motion: moreover, the question arises as to why the differences between Figure 11(A) and Figure 11(B) are so stark when the interface shape and resolution is broadly similar?

An alternative, if somewhat crude, explanation for the presence of these anomalous velocities could proceed thus. Consider a simple, planar, interface between a gas phase and a liquid phase, and suppose that this interface is discretised into *N* equally-sized volumes, of characteristic length Δx, such that the phase fraction, α, varies $0 \leq \alpha \leq 1$. For a Newtonian fluid, the shear stress, τ, is related to the velocity gradient, du/dx, *via* the viscosity, $\bar{\mu}$, *viz*

$$\tau = \bar{\mu}\frac{du}{dx} \tag{12}$$

If it is assumed that the stress, τ, is constant across the interface, the velocity in an arbitrary volume in the interface region, u_{i+1}, can be related to the velocity in the volume preceding it, u_i. Since α varies as a function of position across the interface, then the value of $\bar{\mu}$ will also vary from volume to volume according to the chosen viscosity law: u_{i+1} can hence be written

$$u_{i+1} = u_i + \frac{\tau}{\bar{\mu}_i}\Delta x \tag{13}$$

A suitable boundary condition for Equation (13) is the velocity in the first interface volume, u_1. A plot of normalised interface velocity, u_i/u_1, as a function of α is given in Figure 12 for $N = 45$, $u_1 = 0.1$ mm/s and $\tau = 1$ Pa.

<FIGURE 12>

It is interesting to note the scale of velocity variation illustrated in Figure 12. For the chosen parameters, which, admittedly, are arbitrary, there is a difference of approximately four orders of magnitude between the interface velocity computed using the arithmetic mean viscosity law and those using the logarithmically-weighted velocity law and the harmonic mean viscosity law. The magnitude of this difference is strongly dependent on the number of discrete interface volumes that are chosen, N, along with Δx, τ and u_1. Regardless of the values that are chosen for these parameters, however, the observation that the velocity change across the interface is smallest for the arithmetic mean viscosity rule, intermediate in size for the logarithmically-weighted viscosity rule and most for the harmonic mean viscosity rule still applies. This analysis, although crude and highly simplified, may offer insight into to the data presented in Figure 11 and may help to explain the convergence difficulties experienced when using the harmonic mean viscosity law.

4.4 Examination of 'crescent moon' bubble structure

A final piece of analysis that can be presented is to use the solutions from the logarithmically-weighted model to give insight into the structure of the 'crescent moon' bubbles that have been observed. One of the 'crescent-moon' bubbles computed for Scenario 2 is shown in Figure 13. The predicted bubble shape in the plane of observation is shown in Figure 13(A); Figure 13(B) shows the predicted bubble shape normal to the plane of observation and Figure 13(C) shows a cross-sectional view of the bubble along the plane $A - A'$.

<FIGURE 13>

These images give information about the structure of the 'crescent moon' bubbles that cannot currently be obtained from experiments. A key observation is that the downstream face of the bubble is concave in two planes. This is evident from the 'crescent moon' shape in Figure 12(A), and the sectional view normal to the observation direction shown in Figure 12(C). This is interesting since it suggests that the overall surface area of the bubble, of importance to mass transfer phenomena, is larger than would be estimated from either of the bubble silhouettes shown in Figure 12(A) and (B), or from experimental photographs. On reflection, the shape shown in Figure 12(C) is not surprising: since the bubble almost spans the flow channel, the gas closest to the channel walls will not be travelling as fast as the gas in the centre of the flow, hence giving rise to concavity.

5. Conclusions

The research presented in this paper has demonstrated that a broad variety of bubble shapes can be produced when the viscosity ratio, λ, and capillary numbers, Ca, are large. Here, $5.5 \times 10^5 < \lambda < 3.9 \times 10^6$ and $2.9 < Ca < 35.9$ respectively. The most striking bubble shape was that of the 'crescent moon': a highly concave bubble having sharply cusped tips.

Simulation of bubble behaviour at high viscosity ratio initially proved challenging. The compressible two-phase flow solver in OpenFOAM, `compressibleInterDyMFoam`, failed to produce predictions of bubble shape that were in good qualitative agreement with experimental observation.

Image analysis conducted on both the experimental and simulation work was able to extract quantitative data pertaining to the motion of two parts of the bubble, the centroid and the front, and also to the shape, in terms of roundness and convexity. When the motion and shape metrics obtained from experimental and simulation work were compared, examination of the coefficients of determination, R^2, confirmed the qualitatively-observed poor match.

Modification of the arithmetic mean viscosity rule implemented within OpenFOAM to a logarithmically-weighted arithmetic mean viscosity significantly improved the ability of the simulations to match the experimental work. For medium- and high-resolution simulations with the modified viscosity rule, $R^2 > 0.9$ for almost all metrics.

An unexpected penalty of using the logarithmically-weighted arithmetic mean viscosity rule was significantly extended simulation times. Preliminary analysis presented in this paper demonstrates that the modified rule gives rise to increased interfacial velocity predictions that, in turn, constrain the simulation timestep.

The simulation study was able to give some insight into the three-dimensional structure of the 'crescent moon' bubbles: it was discovered that they exhibit convexity in two mutually orthogonal planes. This level of structural information was not obtainable from the experimental work since observations could only be made of the two-dimensional bubble silhouette.

6. Acknowledgements

Thanks are due to Dr Jie Li for useful discussions, Mr Greville Wilde and his team for hosting the Linux cluster at the West Cambridge Data Centre, and Mr Peter Davidson for initiating the project. Funding is gratefully acknowledged from the EPSRC, grant EP/N00230X/1.

7. Attributions

The experiments and image analysis were done by CHC. Numerical simulations and modifications to OpenFOAM were done by BH. The Linux cluster was built and maintained by BH. The figures were drawn by BH and the text written by BH and JFD. The project was conceived and managed by BH and JFD.

Nomenclature

Roman letters

a	-	Duct width	(m)
b	-	Duct breadth	(m)
$\mathbf{F_i}$	-	Interfacial force vector	(N/m^3)
f	-	Numerically-predicted parameter value	(various)
N	-	Number of discrete interface volumes	(-)
n	-	Summation parameter	(-)
p	-	Pressure	(Pa)
Q	-	Volumetric flow rate of continuous phase	(m^3/s)
R^2	-	Coefficient of determination	(-)
t	-	Time	(s)
Δt	-	Time step	(s)
$\bar{u}$	-	Average velocity	(m/s)
u	-	Scalar velocity	(m/s)
$\mathbf{v}$	-	Velocity vector	(m/s)
Δx	-	Length step	(m)
x	-	Length in the *x*-direction	(m)
$\bar{y}$	-	Arithmetic mean of experimental parameters	(various)
y	-	Experimentally-measured parameter value	(various)

Greek letters

α	-	Phase fraction parameter	(-)
$\boldsymbol{\kappa}$	-	Interface curvature	(-)
λ	-	Viscosity ratio	(-)
$\bar{\mu}$	-	Viscosity weighted by phase field	(Pa s)

μ_g	-	Gas phase viscosity	(Pa s)
μ_l	-	Liquid phase viscosity	(Pa s)
σ	-	Interfacial tension	(N/m)
$\bar{\rho}$	-	Density weighted by phase field	(kg/m^3)
ρ_g	-	Gas density	(kg/m^3)
ρ_l	-	Liquid density	(kg/m^3)
τ	-	Shear stress	(Pa

Dimensionless groups

Ca	-	Capillary number, $\mu u/\sigma$	(-)
Co	-	Courant number, $u\Delta t/\Delta x$	(-)

References

1 Mader HM, Llewellin EW, Mueller SP. The rheology of two-phase magmas: A review and analysis. *J Volcanol Geotherm Res* 2013; **257**: 135–158.

2 Amran YHM, Farzadnia N, Abang Ali AA. Properties and applications of foamed concrete; a review. *Constr Build Mater* 2015; **101**: 990–1005.

3 Mezzenga R, Schurtenberger P, Burbidge A, Michel M. Understanding foods as soft materials. *Nat Mater* 2005; **4**: 729–740.

4 Collishaw PG, Evans JRG. An assessment of expressions for the apparent thermal conductivity of cellular materials. *J Mater Sci* 1994; **29**: 2261–2273.

5 Wallis GB. The terminal speed of single drops or bubbles in an infinite medium. *Int J Multiph Flow* 1974; **1**: 491–511.

6 Richardson JF, Zaki WN. The sedimentation of a suspension of uniform spheres under conditions of viscous flow. *Chem Eng Sci* 1954; **3**: 65–73.

7 Ostwald W. Studien uber die Bildung und Umwandlung fester Koerper. *Zeitschrift fur Phys Chemie* 1897; **22**: 189–330.

8 Voorhees PW. The Theory of Ostwald Ripening. *J Stat Phys* 1985; **38**: 231–252.

9 Prince MJ, Blanch HW. Bubble coalescence and break-up in air-sparged bubble columns. *AIChE J* 1990; **36**: 1485–1499.

10 Rust AC, Manga M. Bubble Shapes and Orientations in Low Re Simple Shear Flow. *J Colloid Interface Sci* 2002; **249**: 476–480.

11 Kameda M, Katsumata T, Ichihara M. Deformation of bubbles in a highly viscous pipe flow. *Fluid Dyn Res* 2008; **40**: 576–584.

12 Kopf-Sill AR, Homsy GM. Bubble motion in a Hele–Shaw cell. *Phys Fluids* 1988; **31**: 18–26.

13 Hinch EJ, Acrivos DA. Long slender drops in a simple shear flow. *J Fluid Mech* 1980; **98**: 305–328.

14 Rallison JM. The Deformation of Small Viscous Drops and Bubbles in Shear Flows. *Annu Rev Fluid Mech* 1984; **16**: 45–66.

15 Pozrikis C. Numerical studies of cusp formation at fluid interfaces in Stokes flow. *J Fluid Mech* 1998; **357**: S0022112097007866.

16 Shikhmurzaev YD. On cusped interfaces. *J Fluid Mech* 1998; **359**: S0022112098008532.

17 Siegel M. Cusp formation for time-evolving bubbles in two-dimensional Stokes flow. *J Fluid Mech* 2000; **412**: S002211200000834X.

18 Khayat RE, Luciani A, Utracki LA, Godbille F, Picot J. Influence of shear and elongation on drop deformation in convergent–divergent flows. *Int J Multiph Flow* 2000; **26**: 17–44.

19 Chung TJ. *Computational Fluid Dynamics*. Cambridge University Press: Cambridge, 2002.

20 Wörner M. Numerical modeling of multiphase flows in microfluidics and micro process engineering: a review of methods and applications. *Microfluid Nanofluidics* 2012; **12**: 841–886.

21 Lörstad D, Fuchs L. High-order surface tension VOF-model for 3D bubble flows with high density ratio. *J Comput Phys* 2004; **200**: 153–176.

22 Hua J, Lou J. Numerical simulation of bubble rising in viscous liquid. *J Comput Phys* 2007; **222**: 769–795.

23 Hua J, Stene JF, Lin P. Numerical simulation of 3D bubbles rising in viscous liquids using a front tracking method. *J Comput Phys* 2008; **227**: 3358–3382.

24 Ohta M, Imura T, Yoshida Y, Sussman M. A computational study of the effect of initial bubble conditions on the motion of a gas bubble rising in viscous liquids. *Int J Multiph Flow* 2005; **31**: 223–237.

25 Carvajal D, Carlesi C, Meléndez-Vejar V, Vásquez-Sandoval D, Monteverde-Videla AHA, Bensaid S. Numerical Simulation of Single-Bubble Dynamics in High-Viscosity Ionic Liquids Using the Level-Set Method. *Chem Eng Technol* 2015; **38**: 473–481.

26 Nekouei M, Vanapalli SA. Volume-of-fluid simulations in microfluidic T-junction devices: Influence of viscosity ratio on droplet size. *Phys Fluids* 2017; **29**. doi:10.1063/1.4978801.

27 Taha T, Cui ZF. CFD modelling of slug flow inside square capillaries. *Chem Eng Sci* 2006; **61**: 665–675.

28 Hoang DA, van Steijn V, Portela LM, Kreutzer MT, Kleijn CR. Benchmark numerical simulations of segmented two-phase flows in microchannels using the Volume of Fluid method. *Comput Fluids* 2013; **86**: 28–36.

29 Khodaparast S, Magnini M, Borhani N, Thome JR. Dynamics of isolated confined air bubbles in liquid flows through circular microchannels: an experimental and numerical study. *Microfluid Nanofluidics* 2015; **19**: 209–234.

30 Mackley MR, Marshall RTJ, Smeulders JBAF. The multipass rheometer. *J Rheol (N Y N Y)* 1995; **39**: 1293–1309.

31 Mackley MR, Hassell DG. The multipass rheometer a review. *J Nonnewton Fluid Mech* 2011; **166**: 421–456.

32 Ranganathan M, Mackley MR, Spitteler PHJ. The application of the multipass rheometer to time-dependent capillary flow measurements of a polyethylene melt. *J Rheol (N Y N Y)* 1999; **43**: 443.

33 Thompson MJ, Pearson JRA, Mackley MR. The effect of droplet extension on the rheology of emulsions of water in alkyd resin. *J Rheol (N Y N Y)* 2001; **45**: 1341–1358.

34 Mackley MR, Moggridge GD, Saquet O. Direct experimental evidence for flow induced fibrous polymer crystallisation occurring at a solid/melt interface. *J Mater Sci* 2000; **35**: 5247–5253.

35 Sonwai S, Mackley MR. The effect of shear on the crystallization of cocoa butter. *J Am Oil Chem Soc* 2006; **83**: 583–596.

36 Lee K, Mackley MR. The application of the multi-pass rheometer for precise rheo-optic characterisation of polyethylene melts. *Chem Eng Sci* 2001; **56**: 5653–5661.

37 Collis MW, Mackley MR. The melt processing of monodisperse and polydisperse polystyrene melts within a slit entry and exit flow. *J Nonnewton Fluid Mech* 2005; **128**: 29–41.

38 Scelsi L, Mackley MR. Rheo-optic flow-induced crystallisation of polypropylene and polyethylene within confined entry–exit flow geometries. *Rheol Acta* 2008; **47**: 895–908.

39 Tuladhar TR, Mackley MR. Experimental observations and modelling relating to foaming and bubble growth from pentane loaded polystyrene melts. *Chem Eng Sci* 2004; **59**: 5997–6014.

40 Sargent M. *The extrusion processing of instant coffee for the purposes of creating a pressurised microstructure*. 2018.https://www.repository.cam.ac.uk/handle/1810/276686 (accessed 8 Jan2019).

41 Delplace F. Laminar flow of Newtonian liquids in ducts of rectangular cross-section a model for both physics and mathematics. *Open Access J Math Theor Phys* 2018; **1**: 198–201.

42 Schindelin J, Arganda-Carreras I, Frise E, Kaynig V, Longair M, Pietzsch T *et al.* Fiji: an open-source platform for biological-image analysis. *Nat Methods* 2012; **9**: 676–682.

43 de Chaumont F, Dallongeville S, Olivo-Marin J-C. ICY: A new open-source community image processing software. In: *2011 IEEE International Symposium on Biomedical Imaging: From Nano to Macro*. IEEE, 2011, pp 234–237.

44 Delgado-Gonzalo R, Uhlmann V, Schmitter D, Unser M. Snakes on a Plane: A perfect snap for bioimage analysis. *IEEE Signal Process Mag* 2015; **32**: 41–48.

45 Williams DJ, Shah M. A Fast algorithm for active contours and curvature estimation. *CVGIP Image Underst* 1992; **55**: 14–26.

46 Mora CF, Kwan AKH. Sphericity, shape factor, and convexity measurement of coarse aggregate for concrete using digital image processing. *Cem Concr Res* 2000; **30**: 351–358.

47 Kvålseth TO. Cautionary Note about R^2. *Am Stat* 1985; **39**: 279–285.

48 Patankar S., Spalding D. A calculation procedure for heat, mass and momentum transfer in three-dimensional parabolic flows. *Int J Heat Mass Transf* 1972; **15**: 1787–1806.

49 Issa R. Solution of the implicitly discretised fluid flow equations by operator-splitting. *J Comput Phys* 1986; **62**: 40–65.

50 So KK, Hu XY, Adams NA. Anti-diffusion method for interface steepening in two-phase incompressible flow. *J Comput Phys* 2011; **230**: 5155–5177.

51 Klostermann J, Schaake K, Schwarze R. Numerical simulation of a single rising bubble by VOF with surface compression. *Int J Numer METHODS FLUIDS Int J Numer Meth Fluids* 2012. doi:10.1002/fld.3692.

52 Brackbill JU, Kothe DB, Zemach C. A continuum method for modeling surface tension. *J Comput Phys* 1992; **100**: 335–354.

53 Patankar S V. *Numerical heat transfer and fluid flow*. Hemisphere Pub. Corp., 1980.

54 Afkhami S, Renardy Y. A volume-of-fluid formulation for the study of co-flowing fluids governed by the Hele-Shaw equations. *Phys Fluids* 2013; **25**: 082001.

55 Courant R, Friedrichs K, Lewy H. On the partial difference equations of mathematical physics. *IBM J Res Dev* 1967; **11**: 215–234.

56 Weller HG, Tabor G, Jasak H, Fureby C. A tensorial approach to computational continuum mechanics using object-oriented techniques. *Comput Phys* 1998; **12**: 620–631.

57 Chen G, Xiong Q, Morris PJ, Paterson EG, Sergeev A, Wang Y-C. OpenFOAM for Computational Fluid Dynamics. *Not AMS* 2014; **61**: 354–363.

58 Pellegrini F, Roman J. Sparse matrix ordering with Scotch. In: *HPCN-Europe 1997. Lecture Notes in Computer Science, vol 1225*. Springer: Berlin, Heidelberg, 1997, pp 370–378.

59 Pellegrini F. Static mapping by dual recursive bipartitioning of process architecture graphs. In: *Proceedings of IEEE Scalable High Performance Computing Conference*. IEEE Comput. Soc. Press, pp 486–493.

60 Ayachit U, Avila LS. *The ParaView guide : updated for ParaView version 4.3*. Kitware Inc., 2015.

61 Lafaurie B, Nardone C, Scardovelli R, Zaleski S, Zanetti G. Modelling Merging and Fragmentation in Multiphase Flows with SURFER. *J Comput Phys* 1994; **113**: 134–147.

62 Harvie DJE, Davidson MR, Rudman M. An analysis of parasitic current generation in Volume of Fluid simulations. *Appl Math Model* 2006; **30**: 1056–1066.

8. Appendix A – calculation of capillary number

Calculation of the capillary number, Equation (1), requires knowledge of a characteristic velocity, u: here, this was taken as the steady-state centre-line velocity in the MPR geometry. Examining Figure 1, it is evident that the cross-section of the MPR is geometry is rectangular at all points. Analytical solutions to the N-S equations have been derived[41] that allow the calculation of the ratio between the centreline velocity and the average velocity, $\bar{u}$, for steady-state, incompressible, laminar flow. For a rectangular duct of width a and breadth b:

$$\frac{u}{\bar{u}} = \frac{2\pi^4 - 64\pi \sum_{n=1,3,5\ldots}^{\infty} \frac{(-1)^{\frac{n-1}{2}}}{\cosh\left(\frac{n\pi b}{2a}\right)}}{128 \sum_{n=1,3,5\ldots}^{\infty} \frac{1}{n^4}\left(1 - \frac{2a}{n\pi b}\tanh\left(\frac{n\pi b}{2a}\right)\right)}$$

(A 1)

It is assumed that the average velocity, $\bar{u}$, can be calculated from the volumetric flow-rate of continuous phase *viz*

$$\bar{u} = \frac{Q}{ab}$$

(A 2)

Estimates of the capillary number in the middle of the orifice, and far away from the orifice are given in Table A 1.

<TABLE A1>

9. List of Tables

Table 1. Geometric data for computational domain shown in Figure 4

Table 2. Mesh data for the computational domain shown in Figure 4.

Table 3. Face definitions for computational domain shown in Figure 4.

Table 4. Physical properties for the gas and liquid phases. Italic numbers denote low viscosity (10 Pa s) properties.

Table 5. Boundary condition definitions for velocity and temperature. Italic number denote inlet velocity for 10 Pa s viscosity cases.

Table 6. Boundary condition definitions for pressure and phase fraction.

Table 7. Initial conditions for preparatory single-phase flow simulation

Table 8. Location, size, and internal pressure of the disperse phase for each of the continuous phase viscosities. Note that the co-ordinate origin was taken as point ***A*** in Table 1.

Table 9. Dynamic mesh refinement parameters for low-, medium- and high-resolution simulations

Table 10. Domain decomposition and solver data.

Table 11. Coefficients of determination for each simulation case.

Table 12. Mesh and timestep data for each simulation

Table A 1. Capillary number estimates.

10. Tables

Table 1. Geometric data for computational domain shown in Figure 4.

Point	Co-ordinates (x, y, z) (mm)	Point	Co-ordinates (x, y, z) (mm)
A	(0,0,0)	A'	(0,0,1)
B	(4.3,0,0)	B'	(4.3,0,1)
C	(5.7,0,0)	C'	(5.7,0,1)
D	(10,0,0)	D'	(10,0,1)
E	(0,5.05,0)	E'	(0,5.05,1)
F	(4.3,5.05,0)	F'	(4.3,5.05,1)
G	(5.7,5.05,0)	G'	(5.7,5.05,1)
H	(10,5.05,0)	H'	(10,5.05,1)
I	(0,6.5,0)	I'	(0,6.5,1)
J	(4.3,6.5,0)	J'	(4.3,6.5,1)
K	(5.7,6.5,0)	K'	(5.7,6.5,1)
L	(10,6.5,0)	L'	(10,6.5,1)
M	(0,11.5,0)	M'	(0,11.5,1)
N	(4.3,11.5,0)	N'	(4.3,11.5,1)
O	(5.7,11.5,0)	O'	(5.7,11.5,1)
P	(10,11.5,0)	P'	(10,11.5,1)

Table 2. Mesh data for the computational domain shown in Figure 4.

Edge segment	Number of edge nodes	Edge grading parameter
$A-B, E-F, I-J, M-N,$	20	$1/3$
$C-D, G-H, K-L, O-P$	20	3
$B-C, F-G, J-K, N-O$	12	1
$A-E, B-F, C-G, D-H$	20	0.5
$F-J, G-K$	12	1
$I-M, J-N, K-O, L-P$	20	2
z-direction, for example $D-D', H-H', L-L', P-P'$ etc.	18	1

Table 3. Face definitions for computational domain shown in Figure 4.

Faces constructed from edge segments	Face name and number
$D-H-G-K-L-P-P'-L'-K'-G'-H'-D'$ $A-E-F-J-I-M-M'-I'-J'-F'-E'-A'$	1 - fixedWalls
$A-B-C-D-D'-C'-B'-A'$	2 - inletVelocity
$M-N-O-P-P'-O'-N'-M'$	3 - outletPressure
$A-B-C-DH-G-K-L-P-O-N-M-I-J-F-E$ $A'-B'-C'-D'-H'-G'-K'-L'-P'-O'-N'-M'-I'-J'-F'-E'$	4 - frontAndBack

Table 4. Physical properties for the gas and liquid phases. Italic numbers denote low viscosity (10 Pa s) properties.

Parameter	Value	Units
Interfacial tension	30	mN/m
Minimum pressure	1×10^5	Pa
Gas phase viscosity	1.84×10^{-5}	Pa
Gas phase Prandtl number	0.7	-
Gas phase heat capacity	1007	J/molK
Gas phase molecular weight	28.9	g/mol
Gas phase density	Calculated using ideal gas law	
Liquid phase viscosity	70 (*10*)	Pa s
Liquid phase Prandtl number	6×10^5	-
Liquid phase heat capacity	1884	J/molK
Liquid phase molecular weight	1260	g/mol
Liquid phase density	890	kg/m^3

Table 5. Boundary condition definitions for velocity and temperature. Italic number denote inlet velocity for 10 Pa s viscosity cases.

Face number	Velocity boundary conditions			Thermal boundary conditions	
	Type	OpenFOAM keyword	Value	Type	OpenFOAM keyword
1	No slip	fixedValue	uniform (0 0 0)	Insulated	zeroGradient
2	Inlet velocity	uniformFixedValue	uniformValue (0 0.000785 0) (*0 0.00785 0*)	Insulated	zeroGradient
3	Outlet boundary	inletOutlet	uniform (0 0 0)	Insulated	zeroGradient
4	No slip	fixedValue	uniform (0 0 0)	Insulated	zeroGradient

Table 6. Boundary condition definitions for pressure and phase fraction.

Face number	Pressure boundary conditions			Phase fraction boundary conditions	
	Type	**OpenFOAM keyword**	**Value**	**Type**	**OpenFOAM keyword**
1	No gradient	zeroGradient		No gradient	zeroGradient
2	No gradient	zeroGradient		No gradient	zeroGradient
3	No gradient	fixedValue	uniform 1e5	No gradient	zeroGradient
4	No gradient	zeroGradient		No gradient	zeroGradient

Table 7. Initial conditions for preparatory single-phase flow simulation

Field	Value	Units
Velocity	(0 0 0)	m/s
Temperature	298	K
Pressure	1×10^5	Pa
Phase fraction	1 (*i.e.* continuous phase)	-

Table 8. Location, size, and internal pressure of the disperse phase for each of the continuous phase viscosities. Note that the co-ordinate origin was taken as point *A* in Table 1.

Parameter	Scenario 1: 70 Pa s continuous phase	Scenario 2: 10 Pa s continuous phase
Bubble centre (x, y, z) (mm)	$(5.09, 3.09, 0.50)$	$(4.80, 2.08, 0.50)$
Bubble radius (mm)	0.37	0.47
Bubble internal pressure (Pa)	1.436×10^5	1.400×10^5

Table 9. Dynamic mesh refinement parameters for low-, medium- and high-resolution simulations

Parameter	Value
Field used for mesh refinement	Phase fraction
Lower refinement level	0.01
Upper refinement level	0.99
Un-refinement level	10
Maximum number of cells	2×10^7
Maximum refinement level (low, medium, high resolution)	2, 3, 4
Number of buffer layers (low, medium, high resolution)	2, 2, 3

Table 10. Domain decomposition and solver data.

Scenario	Viscosity rule	Solution resolution	Number of x domains	Number of y domains	Number of z domains	Courant number (max, min)	Solution end time (s)
1	Arithmetic mean	High	2	1	80	(1.0, 0.1)	1.5
	Logarithmic weighting	Low	1	1	64	(1.0, 0.1)	1.5
	Logarithmic weighting	Medium	1	1	90	(1.0, 0.1)	1.5
	Logarithmic weighting	High	2	1	80	(1.0, 0.1)	1.0
2	Arithmetic mean	High	1	1	90	(0.5, 0.1)	0.15
	Logarithmic weighting	Low	1	1	90	(1.0, 0.1)	0.15
	Logarithmic weighting	Medium	1	1	90	(1.0, 0.1)	0.15
	Logarithmic weighting	High	2	1	80	(1.0, .01)	0.15

Table 11. Coefficients of determination for each simulation case.

Scenario	Viscosity rule	Solution resolution	Coefficient of determination, R^2			
			Centre of bubble	Front of bubble	Roundness	Convexity
1	Arithmetic mean	High	0.889	0.562	0.195	0.540
	Logarithmic weighting	Low	0.994	0.972	0.799	0.643
	Logarithmic weighting	Medium	0.988	0.994	0.919	0.902
	Logarithmic weighting	High	0.985	0.880	0.912	0.985
2	Arithmetic mean	High	0.889	0.594	-0.145	0.732
	Logarithmic weighting	Low	0.937	0.915	0.404	0.740
	Logarithmic weighting	Medium	0.958	0.933	0.648	0.853
	Logarithmic weighting	High	0.966	0.903	0.734	0.898

Table 12. Mesh and timestep data for each simulation

Scenario	Viscosity rule	Solution resolution	Average timestep (s)	Number of iterations	Maximum number mesh cells	Number of cores	Total compute time (hours)
1	Arithmetic mean	High	2.00×10^{-4}	7520	2163664	160	16.9
	Logarithmic weighting	Low	1.04×10^{-5}	144189	103830	64	17.1
	Logarithmic weighting	Medium	3.83×10^{-6}	391462	316868	90	154.1
	Logarithmic weighting	High	1.55×10^{-6}	646419	1376235	160	1075.9
2	Arithmetic mean	High	1.48×10^{-5}	10103	2622339	90	35.6
	Logarithmic weighting	Low	1.2×10^{-5}	12542	141938	90	2.7
	Logarithmic weighting	Medium	4.95×10^{-6}	30313	530921	90	18.6
	Logarithmic weighting	High	1.77×10^{-6}	84660	2386579	160	236.0

Table A 1. Capillary number estimates

Scenario	Volumetric flow-rate (mm^3/s)	Viscosity (Pa s)	Interfacial tension (mN/m)	Location	Duct width, a (mm)	Duct breadth, b (mm)	$\frac{u}{\bar{u}}$	Ca
1	7.85	70	30	Orifice	1.5	1	2.06	25.1
				Far from orifice	10	1	1.60	2.9
2	78.5	10	30	Orifice	1.5	1	2.06	35.9
				Far from orifice	10	1	1.60	4.2

11. List of Figures

Figure 1. Schematic diagram of (A) the multipass rheometer (MPR) showing the location of the orifice (black) and the test fluid (white); (B) the orifice plate used in the experiments.

Figure 2. Schematic diagram of (A) percentage roundness measurement, expressed as $\mathbf{100} \times \boldsymbol{R_1/R_2}$, and (B) percentage convexity measurement, expressed as $\mathbf{100} \times \boldsymbol{A_1/A_2}$.

Figure 3. Plot of viscosity as a function of the phase fraction, $\boldsymbol{\alpha}$. The dashed red line denotes the arithmetic mean viscosity rule, the dotted purple line the harmonic mean viscosity and the solid blue line the arithmetic mean of the natural logarithm of the viscosity.

Figure 4. (A) Schematic diagram of geometry used to generate the finite volume mesh in plan and side views: the locations refer to dimensions shown in Table 1(B) Initial finite volume mesh prior to dynamic refinement based on interface location.

Figure 5. Comparison between photographs of bubble shape (left column) and prediction of bubble shape from computational simulation. In this diagram, blue outlined images correspond to the standard solver at high resolution; green outlined images to the modified solver at low resolution; purple outlined images to the modified solver at medium resolution and red outlined images to the modified solver at high resolution. The viscosity of the liquid surrounding the bubble is 70 Pa s, and flow is from bottom to top. Simulation time is included for comparison.

Figure 6. Plot of (A) the position of the bubble centroid and (B) the position of the front of the bubble as a function of time for a single bubble suspended in a liquid of viscosity 70 Pa s flowing upwards through the orifice shown in Figure 1(B) at a volumetric flow rate of 7.85 mm^3/s. Open circles denote experimental data; the solid black denotes the standard solver at high resolution; the red short-dashed line the modified solver at low resolution; the red long-dashed line the modified solver at medium resolution and the red dotted line the modified solver at high resolution. All data has been shifted such that $\boldsymbol{y = 0}$ mm at $\boldsymbol{t = 0}$ s.

Figure 7. Plot of (A) bubble roundness and (B) bubble convexity as a function of time for a single bubble suspended in a liquid of viscosity 70 Pa s flowing upwards through the orifice shown in Figure 1(B) at a volumetric flow rate of 7.85 mm^3/s. Open circles denote experimental data; the solid black denotes the standard solver at high resolution; the red short-dashed line the modified solver at low resolution; the red long-dashed line the modified solver at medium resolution and the red dotted line the modified solver at high resolution.

Figure 8. Comparison between photographs of bubble shape (left column) and prediction of bubble shape from computational simulation. In this diagram, blue outlined images correspond to the standard solver at high resolution; green outlined images to the modified solver at low resolution; purple outlined images to the modified solver at medium resolution and red outlined images to the modified solver at high resolution. The viscosity of the liquid surrounding the bubble is 10 Pa s, and flow is from bottom to top. Simulation time is included for comparison.

Figure 9. Plot of (A) the position of the bubble centroid and (B) the position of the front of the bubble as a function of time for a single bubble suspended in a liquid of viscosity 10 Pa s flowing upwards through the orifice shown in Figure 1(B) at a volumetric flow rate of 78.5 mm^3/s. Open circles denote experimental data; the solid black denotes the standard solver at high resolution; the red short-dashed line the modified solver at low resolution; the red long-dashed line the modified solver at medium resolution and the red dotted line the modified solver at high resolution. All data has been shifted such that $\boldsymbol{y = 0}$ mm at $\boldsymbol{t = 0}$ s.

Figure 10. Plot of (A) bubble roundness and (B) bubble convexity as a function of time for a single bubble suspended in a liquid of viscosity 10 Pa s flowing upwards through the orifice shown in Figure 1(B) at a volumetric flow rate of 78.5 mm^3/s. Open circles denote experimental data; the solid black denotes the standard solver at high resolution; the red short-dashed line the modified solver at low resolution; the red long-dashed line the modified solver at medium resolution and the red dotted line the modified solver at high resolution.

Figure 11. Velocity field data from numerical simulation (shown as arrows where the length of the arrow is directly proportional to velocity magnitude) superimposed onto the predicted location of a bubble. Flow is from bottom to top. (A) corresponds to the existing solver and (B) the modified solver. Note the presence of significant spurious currents in the modified solved and that the velocity magnitudes of these currents are significantly larger than the velocities in the centre of the orifice.

Figure 12. Variation of normalised velocity as a function of phase fraction for a constant-stress interface using viscosity predictions from (i) the arithmetic mean, Equation (3), dashed red line; (ii) the harmonic mean), Equation (7), solid blue line and (iii) the logarithmically-weighted arithmetic mean, Equation (8), dotted purple line.

Figure 13. Numerical simulation of the silhouette of a ‘crescent-moon’ bubble (A) in the experimental plane of observation; (B) normal to the plane of experimental observation. (C) A cross-section of the bubble at position $\boldsymbol{A - A'}$ showing convexity normal to the plane of observation – information that is not easily obtained experimentally.

12. Figures

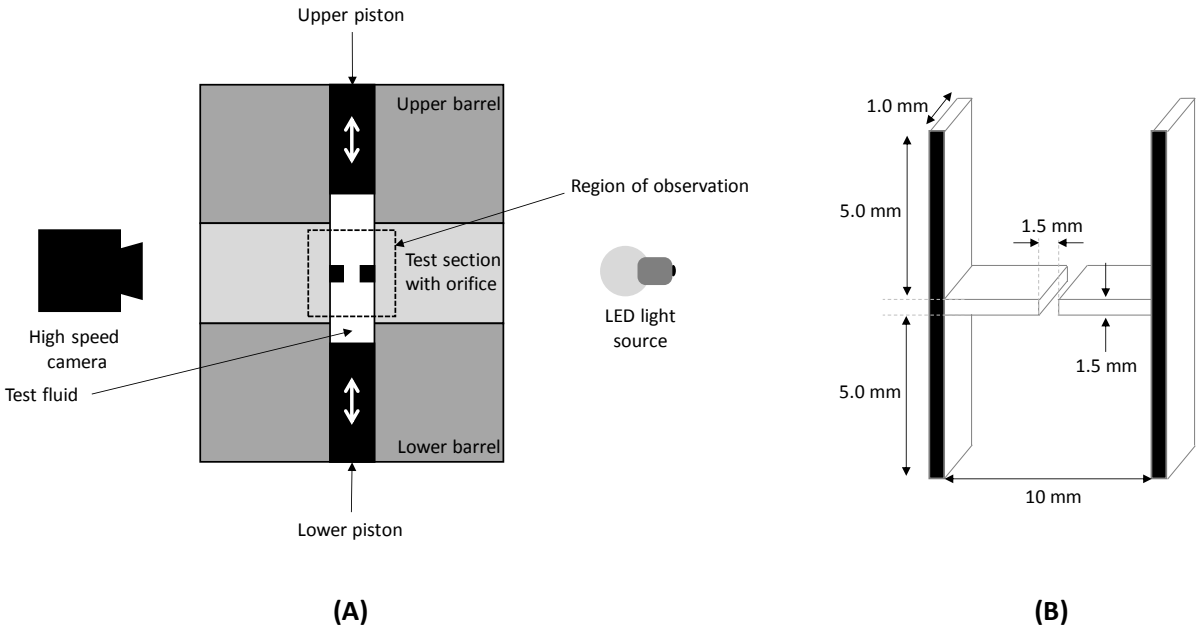

Figure 1. Schematic diagram of (A) the multipass rheometer (MPR) showing the location of the orifice (black) and the test fluid (white); (B) the orifice plate used in the experiments.

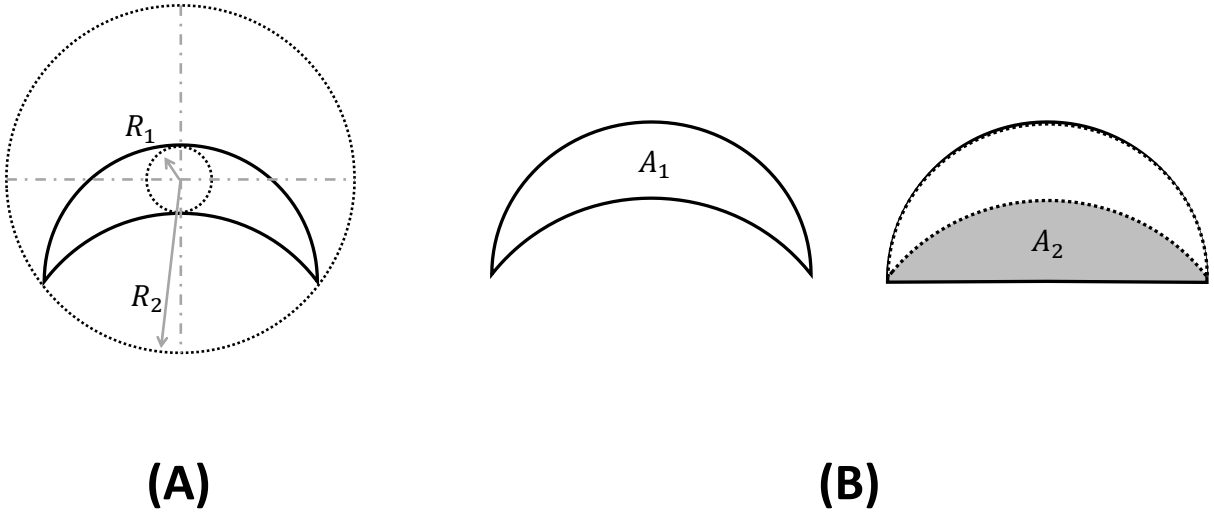

Figure 2. Schematic diagram of (A) percentage roundness measurement, expressed as $100 \times R_1/R_2$, and (B) percentage convexity measurement, expressed as $100 \times A_1/A_2$.

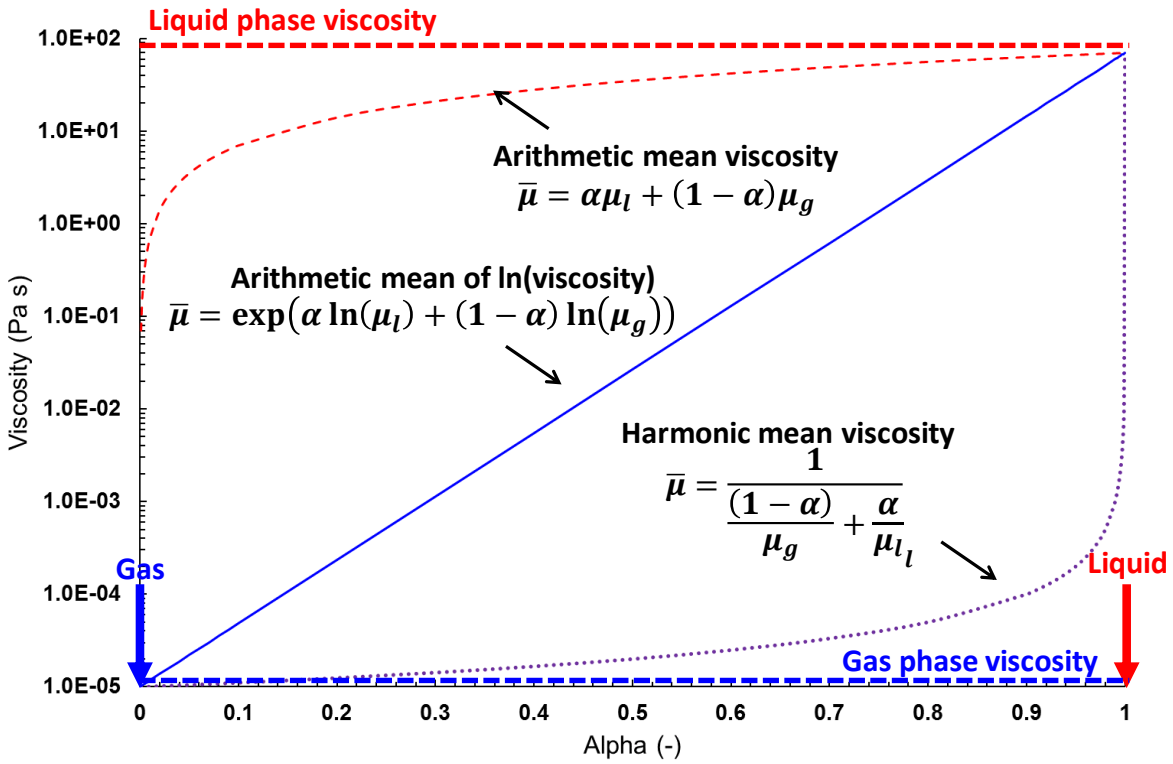

Figure 3. Plot of viscosity as a function of the phase fraction, α. The dashed red line denotes the arithmetic mean viscosity rule, the dotted purple line the harmonic mean viscosity and the solid blue line the arithmetic mean of the natural logarithm of the viscosity.

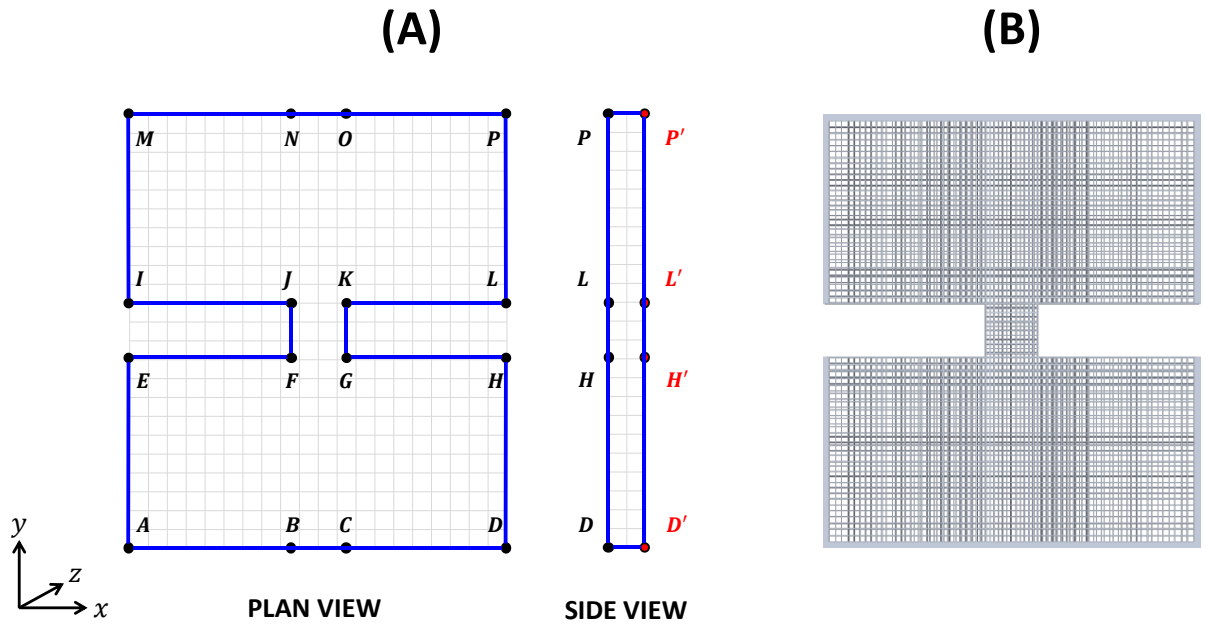

Figure 4. (A) Schematic diagram of geometry used to generate the finite volume mesh in plan and side views: the locations refer to dimensions shown in Table 1(B) Initial finite volume mesh prior to dynamic refinement based on interface location.

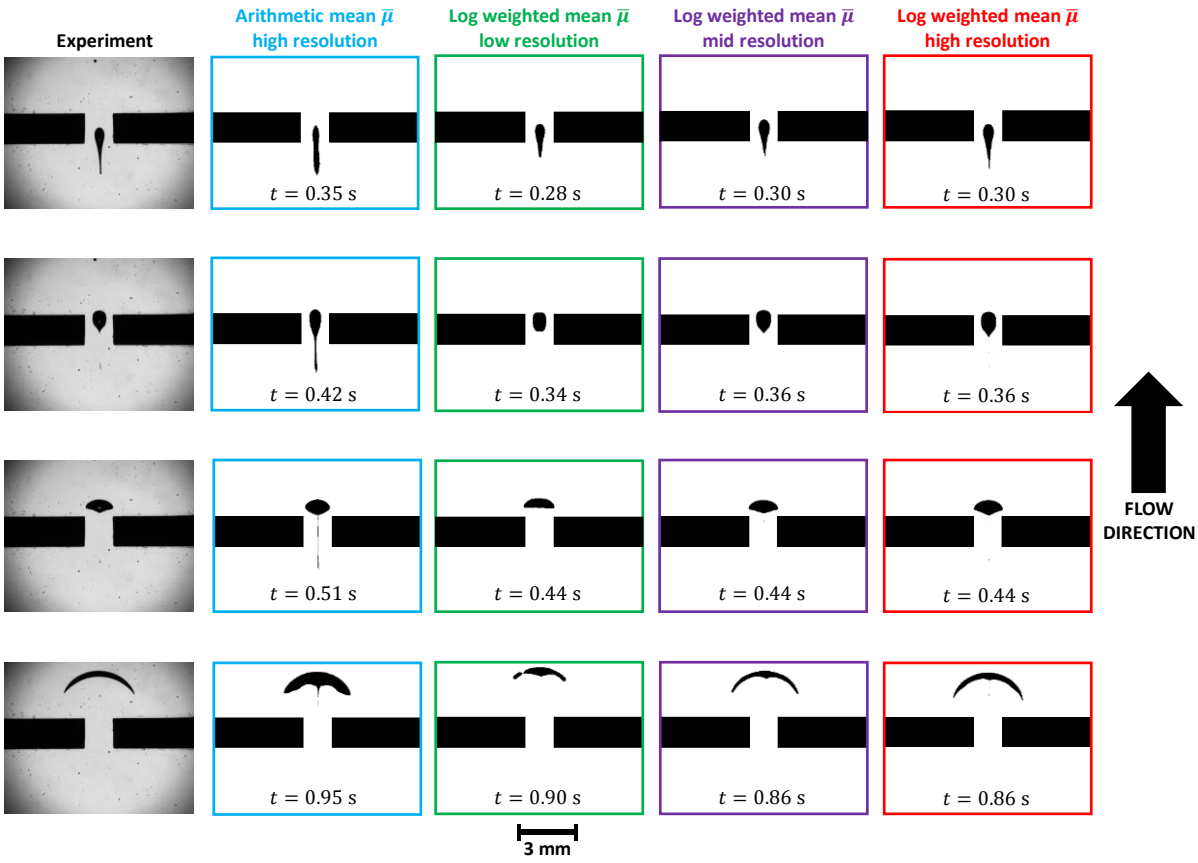

Figure 5. Comparison between photographs of bubble shape (left column) and prediction of bubble shape from computational simulation. In this diagram, blue outlined images correspond to the standard solver at high resolution; green outlined images to the modified solver at low resolution; purple outlined images to the modified solver at medium resolution and red outlined images to the modified solver at high resolution. The viscosity of the liquid surrounding the bubble is 70 Pa s, and flow is from bottom to top. Simulation time is included for comparison.

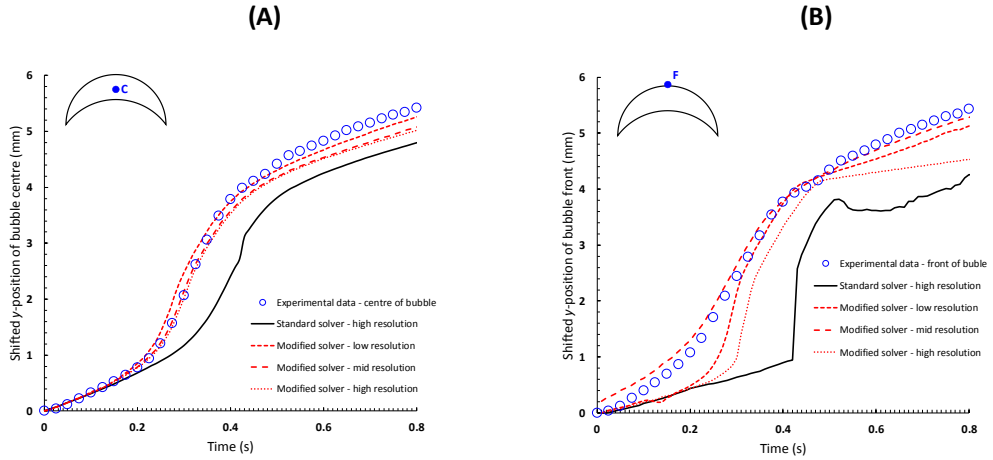

Figure 6. Plot of (A) the position of the bubble centroid and (B) the position of the front of the bubble as a function of time for a single bubble suspended in a liquid of viscosity 70 Pa s flowing upwards through the orifice shown in Figure 1(B) at a volumetric flow rate of 7.85 mm^3/s. Open circles denote experimental data; the solid black denotes the standard solver at high resolution; the red short-dashed line the modified solver at low resolution; the red long-dashed line the modified solver at medium resolution and the red dotted line the modified solver at high resolution. All data has been shifted such that $y = 0$ mm at $t = 0$ s.

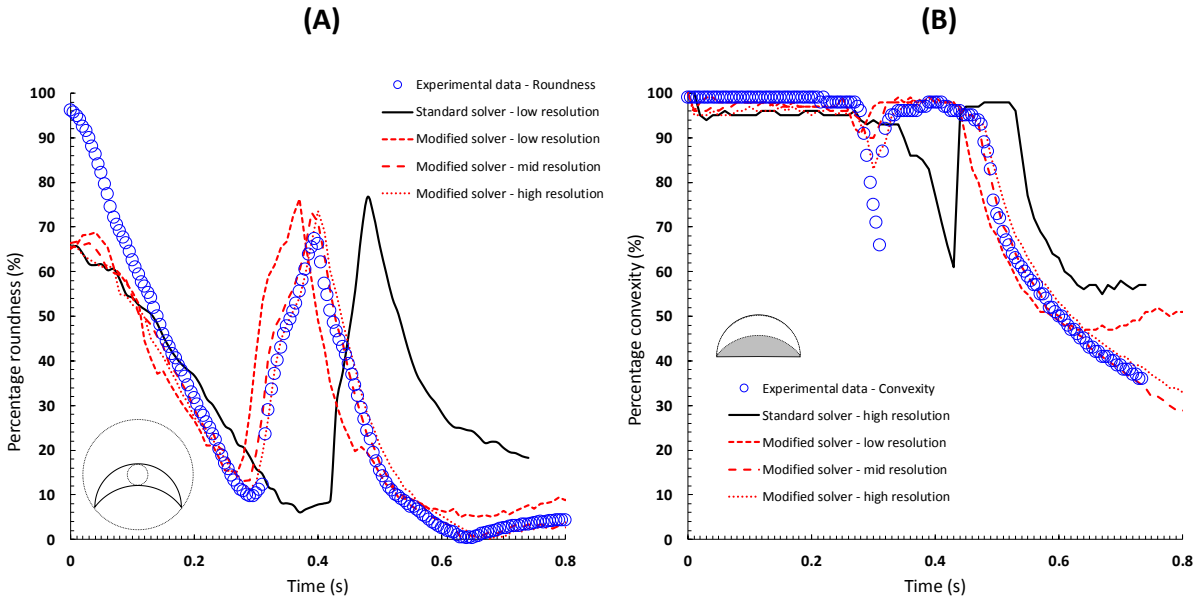

Figure 7. Plot of (A) bubble roundness and (B) bubble convexity as a function of time for a single bubble suspended in a liquid of viscosity 70 Pa s flowing upwards through the orifice shown in Figure 1(B) at a volumetric flow rate of 7.85 mm^3/s. Open circles denote experimental data; the solid black denotes the standard solver at high resolution; the red short-dashed line the modified solver at low resolution; the red long-dashed line the modified solver at medium resolution and the red dotted line the modified solver at high resolution.

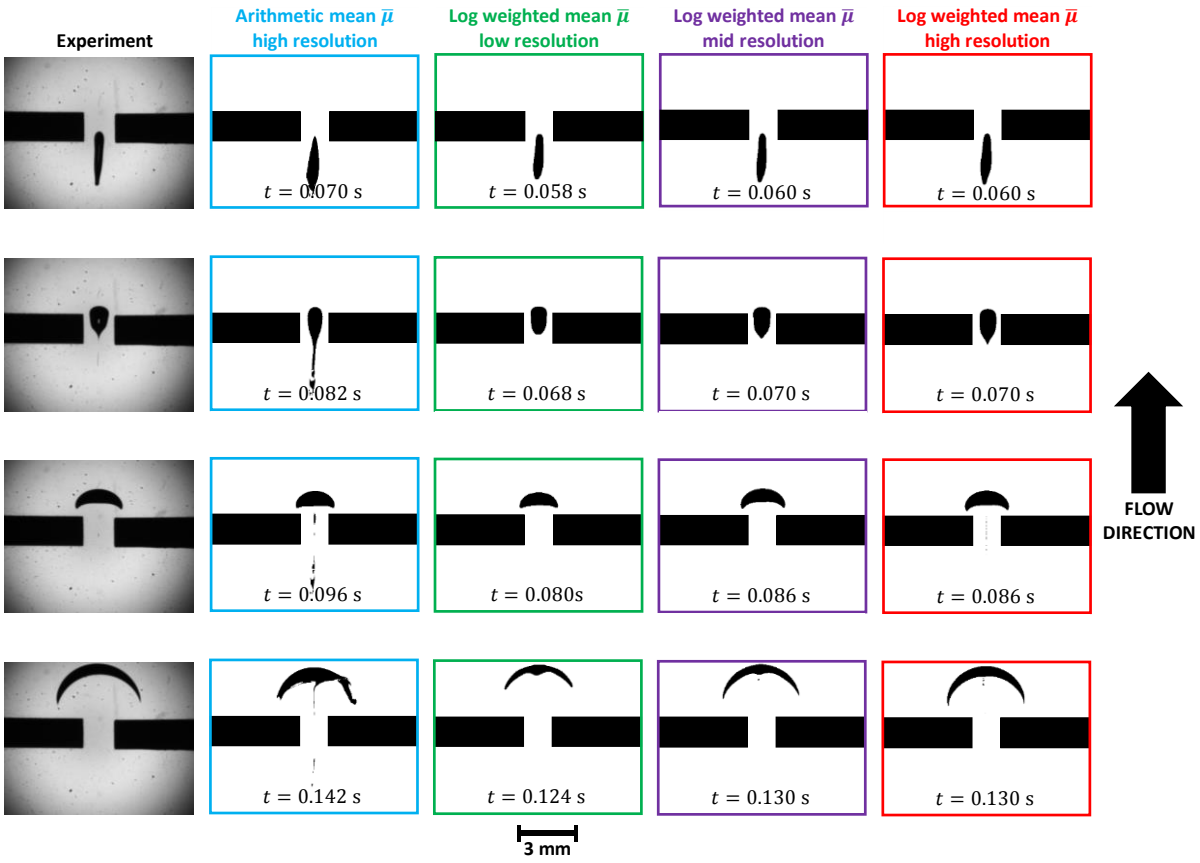

Figure 8. Comparison between photographs of bubble shape (left column) and prediction of bubble shape from computational simulation. In this diagram, blue outlined images correspond to the standard solver at high resolution; green outlined images to the modified solver at low resolution; purple outlined images to the modified solver at medium resolution and red outlined images to the modified solver at high resolution. The viscosity of the liquid surrounding the bubble is 10 Pa s, and flow is from bottom to top. Simulation time is included for comparison.

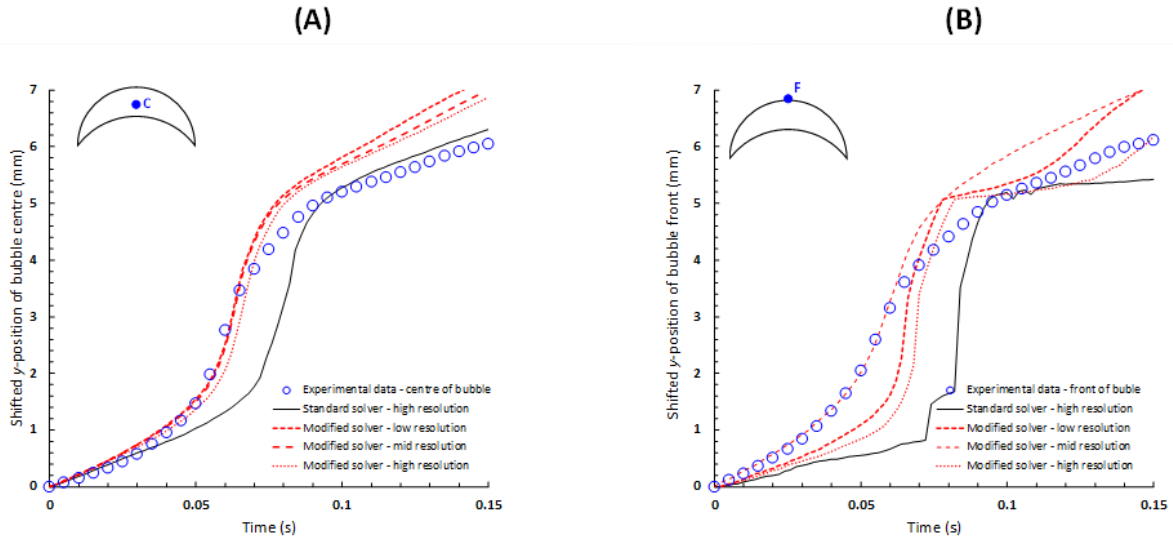

Figure 9. Plot of (A) the position of the bubble centroid and (B) the position of the front of the bubble as a function of time for a single bubble suspended in a liquid of viscosity 10 Pa s flowing upwards through the orifice shown in Figure 1(B) at a volumetric flow rate of 78.5 mm^3/s. Open circles denote experimental data; the solid black denotes the standard solver at high resolution; the red short-dashed line the modified solver at low resolution; the red long-dashed line the modified solver at medium resolution and the red dotted line the modified solver at high resolution. All data has been shifted such that $y = 0$ mm at $t = 0$ s.

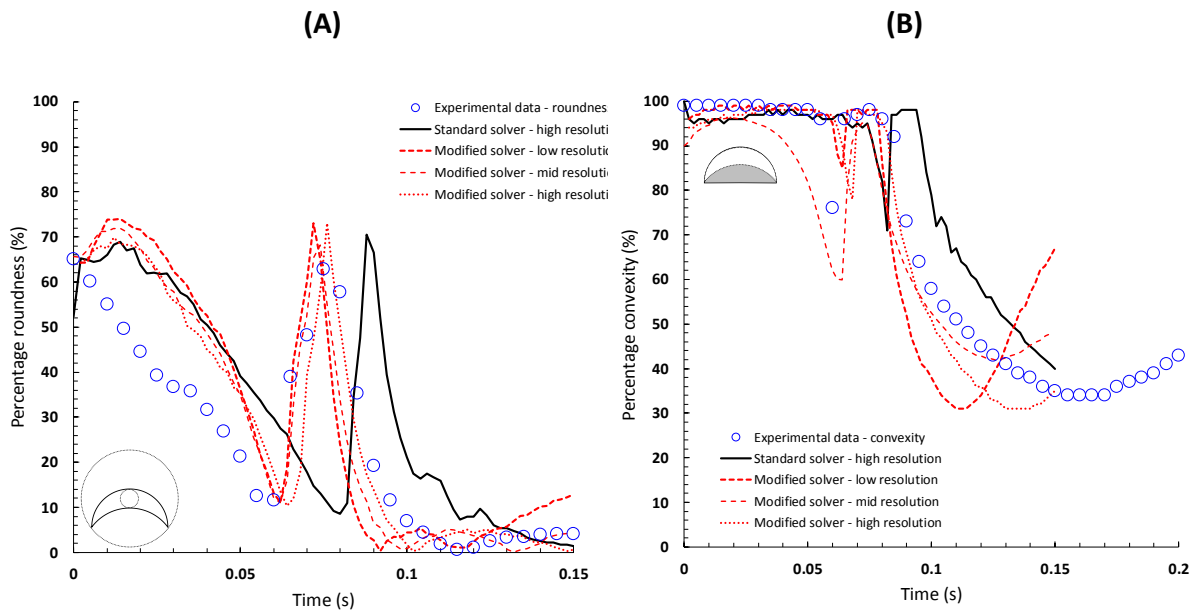

Figure 10. Plot of (A) bubble roundness and (B) bubble convexity as a function of time for a single bubble suspended in a liquid of viscosity 10 Pa s flowing upwards through the orifice shown in Figure 1(B) at a volumetric flow rate of 78.5 mm^3/s. Open circles denote experimental data; the solid black denotes the standard solver at high resolution; the red short-dashed line the modified solver at low resolution; the red long-dashed line the modified solver at medium resolution and the red dotted line the modified solver at high resolution.

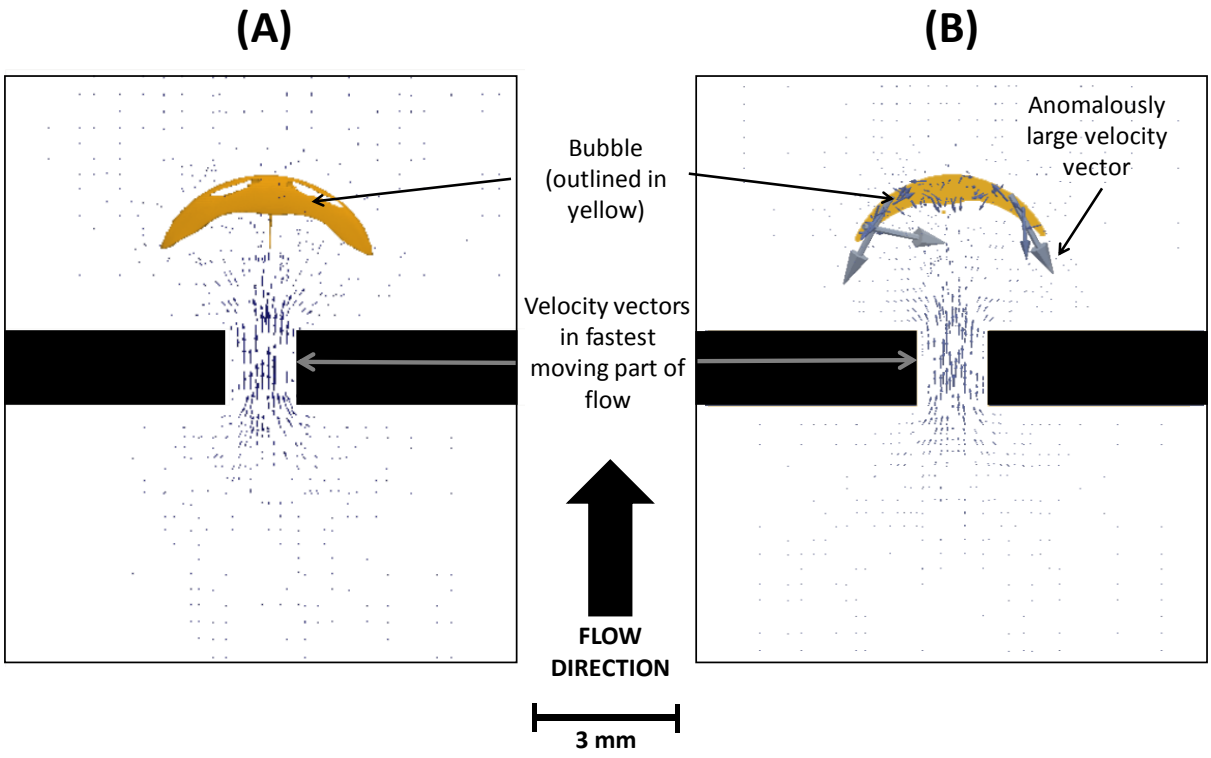

Figure 11. Velocity field data from numerical simulation (shown as arrows where the length of the arrow is directly proportional to velocity magnitude) superimposed onto the predicted location of a bubble. Flow is from bottom to top. (A) corresponds to the existing solver and (B) the modified solver. Note the presence of significant spurious currents in the modified solved and that the velocity magnitudes of these currents are significantly larger than the velocities in the centre of the orifice.

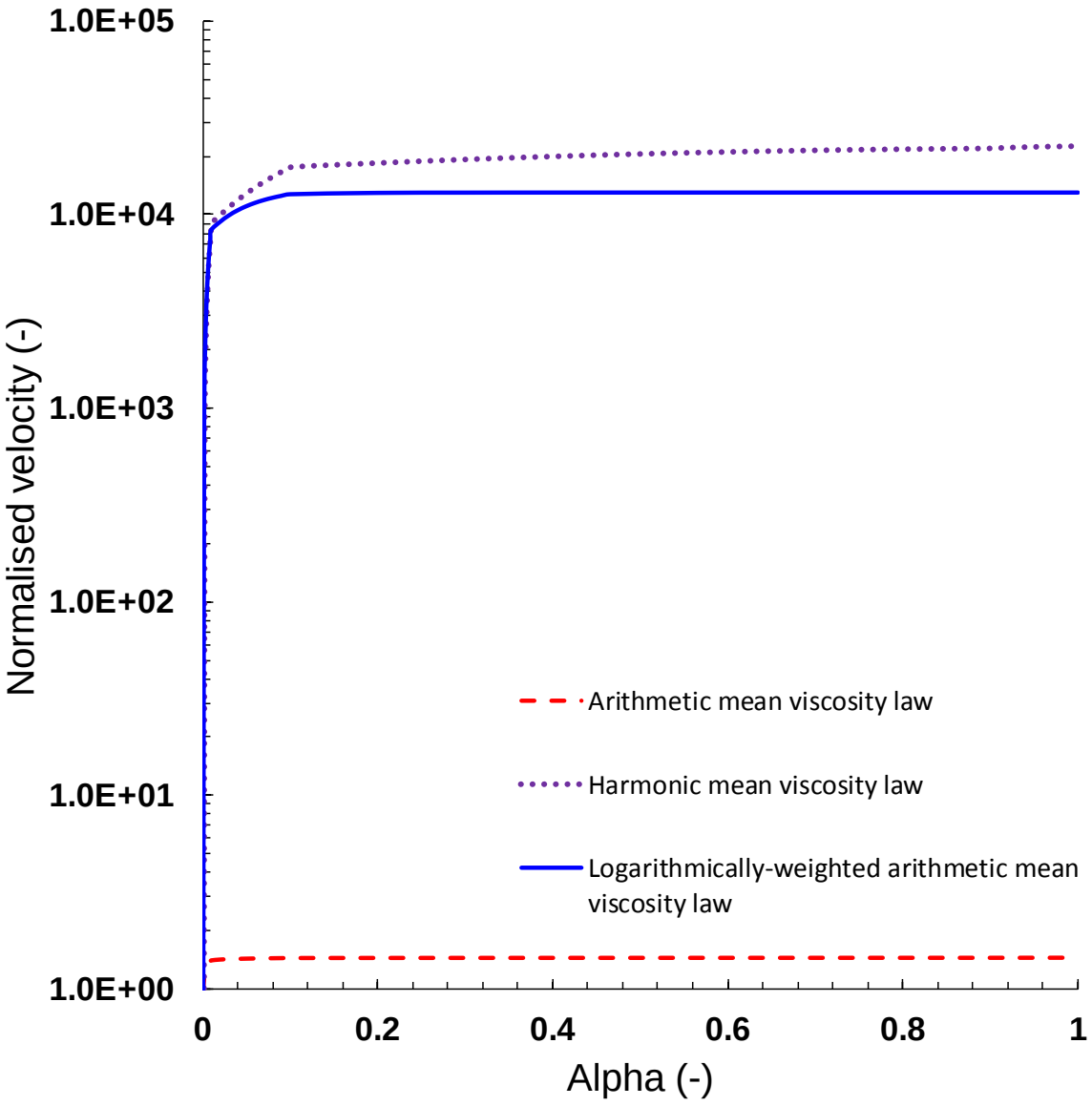

Figure 12. Variation of normalised velocity as a function of phase fraction for a constant-stress interface using viscosity predictions from (i) the arithmetic mean, Equation (3), dashed red line; (ii) the harmonic mean), Equation (7), solid blue line and (iii) the logarithmically-weighted arithmetic mean, Equation (8), dotted purple line.

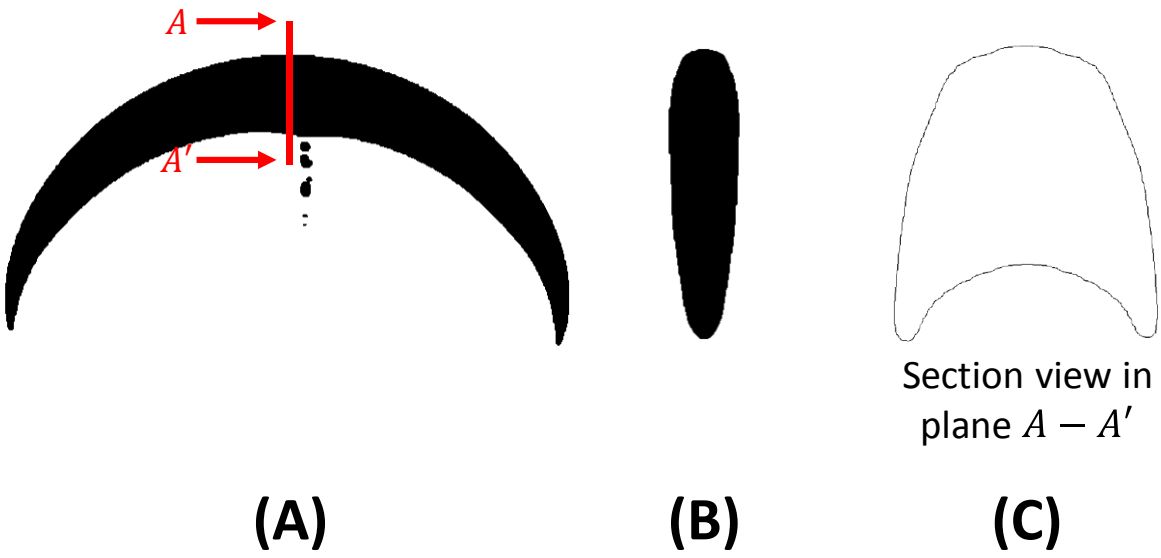

Figure 13. Numerical simulation of the silhouette of a 'crescent-moon' bubble (A) in the experimental plane of observation; (B) normal to the plane of experimental observation. (C) A cross-section of the bubble at position $A - A'$ showing convexity normal to the plane of observation – information that is not easily obtained experimentally.